Incorporation of hydrogen in cubic and uniaxial oxidic crystals deduced from polarized Raman scattering

S. Klauer and M. Wöhlecke

Department of Physics, University of Osnabrück, P.O. Box 4469, D-49069 Osnabrück, Federal Republic of Germany
(Received 2 March 1993; revised manuscript received 17 September 1993)

Polarized Raman scattering investigations of the ir OH stretch mode vibration have been performed in a variety of prototype oxidic crystals, $KTaO_3$, $SrTiO_3$, $K_{1-x}Li_xTaO_3$, TiO_2, $LiTaO_3$, with the aim of providing information on the sites of the incorporation of hydrogen. The traditionally used polarized ir absorption is limited by ensemble averages and its lacking sensitivity to crystallographic orientations of defects. Contrarily Raman scattering is sensitive to the *symmetry* of the dynamical mode. The problem of extracting information on a single defect from an ensemble is treated in the behavior-type theory, which has been developed recently for defects in cubic crystals and was extended to tetragonal and trigonal crystals in the course of these investigations. The principles of the method and the extensive tables are summarized. We describe an experimental method for determining the precise optical alignment of the scattering geometry. In the cubic phase of the perovskites $SrTiO_3$ and $KTaO_3$ with isotropic ir absorption, the Raman data allow us to reject one out of three models, where the protons vibrate between the two next-nearest oxygen ions along the cubic axes, by excluding the related $C_2[100]$ symmetry. In tetragonal $SrTiO_3$ the absorption band splits into three components. In the second model the protons vibrate between the O^{2-} and the Sr^{2+} ions on the face diagonal of the cube, in the last along the edges of the oxygen octahedron between the two nearest-neighbor oxygen ions. The second model can be rejected, because the claimed vertical mirror plane $\sigma(010)$ is not observed in the Raman spectra. The third model claims no mirror symmetry because of the tilting of the octahedra. In $K_{1-x}Li_xTaO_3$, $x=0.023$, a polar tetragonal phase occurs due to the off-center freezing of the Li_K ions along the polar axis. Again three subbands of the OH mode occur. But the bands, which reflected the breakdown of the $\sigma(010)$ symmetry in $SrTiO_3$, do not occur in $K_{1-x}Li_xTaO_3$. The observed vertical mirror plane $\sigma(010)$ reflects the nontilted arrangement of the octahedra in $K_{1-x}Li_xTaO_3$. In TiO_2 (rutile) the Raman data reveal a $C_{1h}(001)$ symmetry for the prominent OH stretch mode. This firmly establishes the model, where the protons vibrate in the center of the open channels between the next-nearest O^{2-} ions in the basal plane. In trigonal $LiTaO_3$ the crystal symmetry is so low that hardly any models can be discriminated on the basis of their symmetry, because most of them deal with C_1 symmetry. This is detected in the experiment and thus any orientation not along the trigonal axis or the vertical mirror plane is compatible with this result. Still one model proposed for $LiNbO_3$ can be excluded.

I. INTRODUCTION

Hydrogen impurities are found in most as-grown oxidic crystals. Their presence can be revealed by the near-ir absorption band of the OH stretch mode. At elevated temperatures the protons may become mobile and contribute to the ionic diffusion and electrical conductivity. Hydrogen may also affect the refractive index. Because of the influence of hydrogen on device applications, it has been the subject of many recent investigations in oxidic materials.

Diffusion and conductivity studies of protons, deuterons, and even tritons in materials such as TiO_2,[1,2] Al_2O_3,[3] $KTaO_3$,[4,5] and $LiNbO_3$ (Refs. 6–8) yielded diffusion constants and activation energies, but weak conclusive evidence for possible hydrogen sites in oxidic lattices. In $LiNbO_3$ the influence of hydrogen on the refractive index is important for applications, such as planar wave guides produced by proton exchange[9] and titanium in-diffusion.[10] The mobile ions, which neutralize the electronic space-charge field during the thermal fixing of holograms in $LiNbO_3$:Fe, were identified to be the pro-

tons.[8,11] Protons also seem to lower the laser optical damage in $LiNbO_3/LiTaO_3$.[12] The point defect chemistry, and the solubility and mobility of protons in alkaline earth titanates of the perovskite structure, e.g., $SrTiO_3$ and $BaTiO_3$, were investigated because of the great technological importance of these materials for electronic ceramics used in passive components.[13]

The infrared absorption of the OH stretch mode provides information on the direction of the OH dipoles and their interaction with the neighboring ions. The ir absorption of a diatomic defect molecule is linearly polarized. The angular dependence of the interaction of the transition dipole moment $\vec{t}_{OH}$, which is parallel to the static dipole moment $\vec{p}_{OH}$, with polarized light $\vec{E}_L$ is determined by the scalar product $\vec{t}_{OH} \cdot \vec{E}_L$. This allows the determination of directions. Most of the information on the directions of each $\vec{p}_{OH}$ is obscured, because the irradiated light interacts with the *ensemble* of energetically degenerate defects, which usually are randomly distributed onto discrete equivalent orientations in the crystal.

This loss of information may eventually be retrieved when either the high symmetry associated with random

distribution is lowered or when the energetic degeneracy of the sites is lifted. In both cases it is necessary to apply an external perturbation, such as an electric or an uniaxial stress field. The first requires a reorientational behavior, but in contrast to paraelectric OH defects in alkali halides[14] none has been observed in oxidic crystals so far to the best of our knowledge. Lifting the energetic degeneracy would lead to a line splitting. A structural phase transition could also cause a line splitting. A good example is $SrTiO_3$ with its prototype antiferrodistortive phase transition at about $T_c \approx 105$ K. The sharp OH absorption band splits into three components in the tetragonal phase below T_c.[15] From extensive ir studies only plausible, not stringent, conclusions could be drawn in favor of the octahedron edge (OE) model.[16] In this model the protons are assumed to vibrate along the O–O edges of the oxygen octahedra. Later on the cube face (CF) model[17,20] was discussed, according to which the protons are believed to vibrate on the face diagonals of the cubic unit cell between the O^{2-} and the Sr^{2+} ion. Unfortunately for each site of the OE model there is a corresponding site of the CF model with the same direction of the OH dipoles, i.e., 45° to the cubic axes. Thus polarized ir absorption is of no further use for the decision making.

However, both models differ with respect to the *local symmetry* of the environment in the crystal. The different symmetry of both models was exploited in a recent polarized Raman investigation.[21] We applied the rather novel Raman behavior-type (BT) method, which was developed in Ref. 22 for the analysis of polarized Raman spectra of defects in *cubic* crystal lattices and reviewed recently. In a reappraisal Raman scattering combined with the BT method is considered as an independent and competitive technique for the determination of the symmetry of defects.[23]

Because of the cubic-tetragonal phase transition in $SrTiO_3$, we had to extend the method to tetragonal systems.[24] The increased discriminative power and the successful application to OH defects stimulated us to examine similar problems in other tetragonal systems, $KTaO_3$:Li (Ref. 21) and TiO_2,[25] as well as to extend both theory and application to still lower symmetric trigonal crystals,[26,27] like the technically important $LiNbO_3/LiTaO_3$ system.

We start with a comparative overview of the capability of the extensions of the BT method to different host crystals. Then the emphasis is put on a comprehensive presentation of the experimental data. In particular the perovskites, represented by $SrTiO_3$, $KTaO_3$, and $KTaO_3$:Li, the TiO_2 as well as the $LiNbO_3/LiTaO_3$ family have been investigated. Each of these families represents a whole class of materials of significant technological interest and in each family there are conflicting models for the sites of hydrogen.

II. THEORY: BEHAVIOR TYPE ANALYSIS OF POLARIZED RAMAN SPECTRA

A. Formalism of the behavior-type method

While applying the Raman behavior-type method a set of extensive tables forms the backbone for the analysis of

Raman spectra of defect modes in cubic crystals.[22] A summary of the capability and successful applications is presented in a recent review.[23]

The polarization dependence of first-order Raman scattering is characterized by a second-rank tensor, which connects the unit electric field polarization vectors $\vec{a} \equiv \hat{E}_{in}$ and $\vec{b} \equiv \hat{E}_{out}$ of the incident and scattered light, respectively,[28]

$$I_{\vec{a},\vec{b}} \propto |\vec{a}\,^t\,\overline{T}\,\vec{b}|^2 . \tag{1}$$

The form of the Raman tensor $\overline{T}$ depends on the symmetry of the dynamical mode, characterized by the point group O'_1 and the irreducible representation Γ', to which the mode belongs. The Raman tensors, expressed in the reference frame of the defect, are listed in Ref. 28.

For lattice modes the transformation properties and thus their Raman tensors can in principle be completely determined. A suitable choice of the polarization vectors $(\vec{a},\vec{b})$ along the rectangular axes of the crystal frame (x,y,z) allows a direct experimental determination of the tensor elements, because according to Eq. (1), we have, e.g., for $(\vec{a},\vec{b})=(x,y)$ that $I_{\vec{a},\vec{b}}=I_{x,y} \propto (T)^2_{xy}$, etc. Polarized measurements of gases and fluids belong to the opposite extreme. They are usually expressed in terms of the two invariants of the symmetric Raman tensor, the average polarizability $\bar{\alpha}$, and the anisotropy γ.[29] Because experiments can only yield relative intensities, the symmetry information is contained in only *one* intensity ratio, usually called the depolarization ratio ρ, which allows a discrimination merely between totally symmetric modes from all the others. Further discrimination between irreducible representations or conclusions concerning the symmetry point group of the molecules are not possible.[28,29]

Local modes (defect modes) in crystals represent a situation between the two extremes. Here, one deals with a finite number of *discrete orientations* of the *single defects* within the crystal. It is the task of the behavior-type method to spell out to what extent information on the irreducible representation and the symmetry, i.e., the form of the Raman tensor of the single defect, can be retrieved after the *ensemble average*.

The detected polarized Raman scattering intensity $I_{\vec{a},\vec{b}}$ is the incoherent superposition of the contributions $I_{\vec{a},\vec{b}}^{(n)}$ of defects with the $n=1,\ldots,h'$ energetically equivalent orientations v_n weighed with the population numbers $N^{(n)}$:

$$I_{\vec{a},\vec{b}} = \sum_{n=1}^{h'} N^{(n)} I_{\vec{a},\vec{b}}^{(n)} . \tag{2}$$

For any arbitrary initial orientation v_1 of a dynamical mode possessing the Raman tensor $\overline{T}^{(1)}$ the orientations v_n and the related Raman tensors $\overline{T}^{(n)}$ of the energetically equivalent modes in the crystal lattice with the symmetry point group G' are generated by the symmetry operations $R_n \in G'$ according to

$$v_n = R_n v_1 \text{ and } \overline{T}^{(n)} = R_n \overline{T}^{(1)} R_n^{-1} . \tag{3}$$

Each orientation contributes the amount

$$I_{\vec{a},\vec{b}}^{(n)} = k I_0 |\vec{a}\,^t\overline{\mathbf{T}}^{(\mathbf{n})}\,\vec{b}|^2 \qquad (4)$$

to the total scattering intensity. Here, I_0 is the intensity of the incident laser beam and k represents the experimental detection efficiency, which accounts for the optical geometry of the experiment, the orientation of the crystal, the quality of the crystal surfaces, etc. A reordering of Eq. (2) allows one to separate the *geometrical factors* of the experiment, which are solely determined by the choice of the polarization vectors $\vec{a}$ and $\vec{b}$, from the *intrinsic quantities* $[N^{(n)}, T_{ij} = (\overline{T}^{(1)})_{ij}]$. These contain all the information on the symmetry of the defect and the distribution onto its orientations v_n:

$$I_{\vec{a},\vec{b}} = \sum_{i=1}^{3}\sum_{j=1}^{3}\sum_{k=1}^{3}\sum_{l=1}^{3} a_i b_j a_k b_l P_{ijkl} \; . \qquad (5)$$

This defines the *intensity parameters* (IP's)

$$P_{ijkl} = k I_0 \sum_{n=1}^{h'} N^{(n)} T_{ij}^{(n)} T_{kl}^{(n)} \; . \qquad (6)$$

For nonresonant Raman scattering $(T_{ij} = T_{ji})$, the amount of 81 IP's defined in Eq. (6) reduces to at maximum 21 *independent quantities* when all the population numbers $N^{(n)}$ and the tensor elements T_{ij} are assumed to be independent. For a better survey we use the shorthand notations $(q_i, r_i, s_i, t_i, u_i, v_i)$ for the IP's introduced in Refs. 22 and 24.

Although the intrinsic quantities $(N^{(n)}, T_{ij})$ could in principle be retrieved by solving the system of equations, with the IP's as the input parameters, this procedure is not practicable, as discussed in Ref. 22. As an alternative the behavior-type method focuses on the existence of simple, symmetry-induced algebraic relations between the IP's. Very often rather simple characteristic relations are induced, such as $x_i = 0$, $x_i = c x_j$, $x_i = c(x_j + x_k)$, $x_i = c(x_j x_k)^{1/2}$, where the x_v $(v = i, j, k)$ represent specific IP's and c is a positive or negative integer or half integer. *The complete set of 21 IP's together with the relations among the IP's is defined as the behavior type (BT) of a mode.*

In this context symmetry accounts for the local symmetry O_1' and the transformation properties Γ' of the mode of the single defect as well as the distribution of the defects onto the orientations. The symmetry of the mode is manifested in relations between the tensor elements T_{ij} and the defect distribution in the population numbers $N^{(n)}$. The complete formalism allows one to treat partial preferential orientation, but here we concentrate on the most relevant case of random distribution, $N^{(1)} = N^{(2)} = \cdots N^{(h')}$. This equality reduces the number of independent IP's to a maximum of 3 for cubic, 5 for tetragonal, and 6 for trigonal crystal symmetry. The relations among the IP's, which are purely induced by random distribution, are called the *minimum BT* for the crystal symmetry G'. This BT holds for a defect with the lowest point symmetry $O_1' = C_1$, i.e., the most general form of the Raman tensor. When the defect symmetry O_1' increases, i.e., when additional relations among the tensor elements T_{ij} are group theoretically required,

more and more algebraic relations are added to the minimum BT.

The variety of possible dynamical modes $(O_1':\Gamma')$ of defects, i.e., their irreducible representations Γ' subject to the actual local symmetry $O_1' \in G'$, is classified into sets of representative modes Γ subject to representative symmetries O_1, such that each representative mode $(O_1:\Gamma)$ corresponds to a characteristic BT. There is a many-to-one mapping of dynamical modes $O_1':\Gamma'$ onto the BT. This is not only because different dynamical modes may possess the same form of the Raman tensor and thus trivially the same BT, but also because of internal symmetries in the explicit expressions of Eqs. (6).[22,24] Dynamical modes belonging to the same representative mode cannot be distinguished further on the basis of the Raman data alone.

It is the idea of the BT method to supply a set of compiled tables, which essentially contain the results of a complete *a priori* calculation of all the BT's for all possible representative modes. An inspection of these tables (e.g., Tables I, II, and IV) reveal that there occur certain actual IP relations, which are characteristic for specific representative defect symmetries O_1. The characteristic IP relations can relatively easily be checked in an experiment. Then the defect symmetries, which correspond to relations not compatible with the observed BT, can be excluded.

We point out that the BT method may not be viewed as a schematic "black box" procedure to analyze polarized Raman data. Limitations occur for two reasons: (i) Because of the many-to-one mapping of the dynamical modes onto the representative modes in general, several possibilities have to be taken into account for each experimentally determined BT. (ii) The symmetry-induced IP relations calculated and discussed so far shall be called *actual BT's*. The IP relations derived from the experiment make up what is called the *observed BT's*. It is important to notice the distinction. It is possible that because of accidental relations among the Raman tensors elements, e.g., because of the specific nature of the dynamical mode or details of the vibronic coupling, certain relations among the IP's are simulated, which may not be required by the actual defect symmetry. This leads to problems when such nearly fulfilled IP relations cannot be excluded stringently due to insufficient experimental accuracy of the polarized intensities. In those cases the observed BT may correspond to a higher symmetry than the actual symmetry. The possibility of this so-called *accidental degeneracy* was investigated for defects in cubic[22] and tetragonal crystals[24] in full detail.

B. BT method in different crystal systems

The point group O_1' of the defect is a subgroup of the crystal point group G'. In order to include all possible dynamical modes $O_1':\Gamma'$ one has to start with the largest crystal point group G' in each crystal system. This is $G' = O_h$ for the cubic crystal system, $G' = D_{4h}$ for the tetragonal system and $G' = D_{3d}$ for the trigonal system.

Partial preferential orientation is treated with an orientating operator $\hat{\mathbf{F}}$ acting on the population numbers. The

population numbers $N(v_n)$ and $N(iv_n)$ of two orientations connected by the inversion i can in principle be influenced differently by $\hat{F}$. But because the Raman tensor is invariant under the inversion, both orientations are treated as partners with a common population number $N^{(n)} = N(v_n) + N(iv_n)$. Therefore, the treatment of $\hat{F}$ is restricted to the subgroup G which generates $G' = G \times I$ according to the direct product with the group $I = \{e, i\}$.[22,24] A reduction from G' to G can also be performed for the variety of all possible dynamical modes. Because of the invariance of $\hat{T}$ under inversion, several modes with different actual defect symmetries $O_1' \subset G'$ reduce to the same representative symmetries $O_1 \subset G$. Together with the irreducible representations Γ of the representative symmetries O_1 one arrives at a classification of the variety of modes $(O_1':\Gamma')$ according to the representative modes $(O_1:\Gamma)$, which the actual behavior types are related to.

1. Cubic crystals

For the case of random distribution and for the most general Raman tensor of a defect with $O_1 = C_1$ one obtains the minimum BT for defects in cubic crystals. This comprises the IP relations

$$q_1 = q_2 = q_3 = q \ ,$$
$$r_1 = r_2 = r_3 = r \ ,$$
$$s_1 = s_2 = s_3 = s \ , \tag{7}$$
$$t_i = u_i = v_j = 0 \quad (i = 1, \ldots, 3, \ j = 1, \ldots, 6) \ .$$

Table I presents an extraction of the extensive tables in Ref. 22 for later applications. It illustrates the classification of 124 possible dynamical modes $(O_1':\Gamma')$ into the 33 subgroups O_1' of O_h into 24 representative modes $(O_1:\Gamma)$ subject to 10 representative symmetries

TABLE I. Cubic crystals. Classification of the 124 possible dynamical modes Γ' of the 33 subgroups O_1' of O_h into 10 representative symmetries O_1 and 24 representative modes Γ. The corresponding BT numbers are from Ref. 22 and the IP relations for a random distribution of defects are given in the last two columns.

Representative symmetry O_1	Representative mode Γ	Dynamical modes $(O_1':\Gamma')$	BT No.	IP relations		
C_1	A	$C_1{:}A \quad S_2{:}A_g$	60	q	r	s
$C_2[010]$	A	$C_2[010]{:}A \quad C_{1h}(010){:}A' \quad C_{2h}[010]{:}A_g$	60	q	r	s
	B	$C_2[010]{:}B \quad C_{1h}(010){:}A'' \quad C_{2h}[010]{:}B_g$	15			s
$C_2[110]$	A	$C_2[110]{:}A \quad C_{1h}(110){:}A' \quad C_{2h}[110]{:}A_g$	60	q	r	s
	B	$C_2[110]{:}B \quad C_{1h}(110){:}A'' \quad C_{2h}[110]{:}B_g$	40	q	$-\frac{1}{2}q$	s
$D_2[100]$	A	$D_2[100]{:}A \quad C_{2v}(100){:}A_1 \quad D_{2h}[100]{:}A_g$	50	q	r	
	B_1	$D_2[100]{:}B_1,B_2,B_3 \quad C_{2v}(100){:}A_2,B_1,B_2 \quad D_{2h}[100]{:}B_{1g},B_{2g},B_{3g}$	15			s
$D_2[110]$	A	$D_2[110]{:}A \quad C_{2v}[1\bar{1}0]{:}A_1 \quad C_{2v}(110){:}A_1 \quad D_{2h}[110]{:}A_g$	60	q	r	s
	B_1	$D_2[110]{:}B_1 \quad C_{2v}[1\bar{1}0]{:}B_1 \quad C_{2v}(110){:}A_2 \quad D_{2h}[110]{:}B_{1g}$	14	q	$-\frac{1}{2}q$	
	B_2	$D_2[110]{:}B_2,B_3 \quad C_{2v}[1\bar{1}0]{:}B_2,A_2 \quad C_{2v}(110){:}B_1,B_2 \quad D_{2h}[110]{:}B_{2g},B_{3g}$	15			s
$C_3[111]$	A	$C_3{:}A \quad S_6{:}A_g$	39	q	q	s
	E	$C_3{:}E \quad S_6{:}E_6$	40	q	$-\frac{1}{2}q$	s
$D_3[111]$	A	$D_3{:}A_1 \quad D_{3d}{:}A_{1g} \quad C_{3v}{:}A_1$	39	q	q	s
	E	$D_3{:}E \quad D_{3d}{:}E_g \quad C_{3v}{:}E$	40	q	$-\frac{1}{2}q$	s
$C_4[001]$	A	$C_4{:}A \quad S_4{:}A \quad C_{4h}{:}A_g$	50	q	r	
	B	$C_4{:}B \quad S_4{:}B \quad C_{4h}{:}B_g$	40	q	$-\frac{1}{2}q$	s
	E	$C_4{:}E \quad S_4{:}E \quad C_{4h}{:}E_g$	15			s
$D_4[001]$	A_1	$D_4{:}A_1 \quad D_{4h}{:}A_{1g} \quad D_{2d}[001]{:}A_1 \quad D_{2d}[110]{:}A_1 \quad C_{4v}{:}A_1$	50	q	r	
	B_1	$D_4{:}B_1 \quad D_{4h}{:}B_{1g} \quad D_{2d}[001]{:}B_1 \quad D_{2d}[110]{:}B_2 \quad C_{4v}{:}B_1$	14	q	$-\frac{1}{2}q$	
	B_2	$D_4{:}B_2 \quad D_{4h}{:}B_{2g} \quad D_{2d}[001]{:}B_2 \quad D_{2d}[110]{:}B_1 \quad C_{4v}{:}B_2$	15			s
	E	$D_4{:}E \quad D_{4h}{:}E_g \quad D_{2d}[001]{:}E \quad D_{2d}[110]{:}E \quad C_{4v}{:}E$	15			s
T	A	$T{:}A \quad T_h{:}A_g \quad O{:}A_1 \quad T_d{:}A_1 \quad O_h{:}A_{1g}$	13	q	q	
	E	$T{:}E \quad T_h{:}E_g \quad O{:}E \quad T_d{:}E \quad O_h{:}E_g$	14	q	$-\frac{1}{2}q$	
	T	$T{:}T \quad T_h{:}T_g \quad O{:}T_2 \quad T_d{:}T_2 \quad O_h{:}T_{2g}$	15			s
$\Sigma = 10$	$\Sigma = 24$	$\Sigma = 124$				

$O_1 \subset O$ and relates them to the cubic BT.

When only one defect mode can be detected, only seven sets of modes can possibly be discriminated, because of seven different BT's for random distribution. This has to be compared with the two distinguishable sets of modes in gases and fluids. The discriminative power may be enhanced when the BT of two or more modes of the same defect can be detected and analyzed, or when partial preferential orientation can lower the high symmetry related to random distribution.

2. Tetragonal crystals

With the arguments of Sec. II B the treatment is reduced, $G' = D_{4h} = G \times I$ to $G = D_4$. The minimum BT (for $O_1 = C_1$) in tetragonal crystals comprises the relations

$$q_1 = q_2 =: q_{1,2}, \quad q_3 ,$$
$$r_1 = r_2 =: r_{1,2}, \quad r_3 ,$$
$$s_1 = s_2 =: s_{1,2}, \quad s_3 , \qquad (8)$$
$$t_i = u_i = v_j = 0 \quad (i = 1, \ldots, 3, \ j = 1, \ldots 6) ,$$
$$(q_{1,2} + r_3) = 2(r_{1,2})^2 / q_3 .$$

It consists of five independent IP's, $q_{1,2}$, q_3, r_3, $s_{1,2}$, and s_3. Note that $r_{1,2}$ is also different from zero in the general case, but not independent from the other five nonzero IP's, because of the last relation of Eqs. (8). The explicit dependences of these IP's from the Raman tensor elements are given by

$$q_{1,2} = 4kI_0[(T_{11})^2 + (T_{22})^2] ,$$
$$q_3 = 8kI_0(T_{33})^2 ,$$
$$r_{1,2} = 4kI_0[T_{11}T_{33} + T_{22}T_{33}] ,$$
$$r_3 = 8kI_0 T_{11}T_{22} , \qquad (9)$$
$$s_{1,2} = 4kI_0[(T_{13})^2 + (T_{23})^2] ,$$
$$s_3 = 8kI_0(T_{12})^2 .$$

The classification of 80 dynamical modes in 25 symmetries $O_1' \subset D_{4h}$ into 20 representative modes with 8 representative symmetries $O_1 \subset D_4$ and the correspondence to 13 different BT's for random distribution in tetragonal crystals is given in Table VI of Ref. 24. The characteristic IP relations of these BT's are provided in Table II.

TABLE II. Listing of all BT's which can occur for a random distribution in tetragonal crystals, corresponding to the representative modes Γ and symmetries O_1 of Table VI in Ref. 24.

O_1	Γ	BT No.	IP relations						
C_1	A	BT 21	q_{12}	q_3	r_{12}	r_3	s_{12}	s_3	a
$C_2[001]$	A	BT 26	q_{12}	q_3	r_{12}	r_3		s_3	a
	B	BT 45					s_{12}		
$C_2[010]$	A	BT 24	q_{12}	q_3	r_{12}	r_3	s_{12}		a
	B	BT 42					s_{12}	s_3	
$C_2[110]$	A	BT 22	q_{12}	q_3	r_{12}	q_1	s_{12}	s_3	b
	B	BT 36	q_{12}			$-q_{12}$	s_{12}		
$D_2[100]$	A	BT 30	q_{12}	q_3	r_{12}	r_3			a
	B_1	BT 46						s_3	
	B_2	BT 45					s_{12}		
$D_2[110]$	A	BT 27	q_{12}	q_3	r_{12}	q_1		s_3	b
	B_1	BT 43	q_{12}			$-q_{12}$			
	B_2	BT 45					s_{12}		
$C_4[001]$	A	BT 33	q_{12}	q_3	r_{12}	q_1			b
	B	BT 38	q_{12}			$-q_{12}$		s_3	
	E	BT 45					s_{12}		
$D_4[001]$	A	BT 33	q_{12}	q_3	r_{12}	q_1			b
	B_1	BT 43	q_{12}			$-q_{12}$			
	B_2	BT 46						s_3	
	E	BT 45					s_{12}		

[a] $(q_{12} + r_3) = (2r_{12}^2 / q_3)$.
[b] $r_{12} = (q_{12}q_3)^{1/2}$.

3. Trigonal crystals

Here the treatment can be reduced to $G = D_3$.[26] The minimum BT contains seven nonzero IP's, six of which are independent:

$$q_1 = q_2 = :q_{1,2}, q_3 ,$$

$$r_1 = r_2 = :r_{1,2}, r_3 ,$$

$$s_1 = s_2 = :s_{1,2}, s_3 ,$$

$$t_1 = u_1 = -v_1 ,$$

$$t_i = u_i = v_j = 0 \quad (i = 2, \ldots, 3, \; j = 2, \ldots, 6) ,$$

$$(q_{1,2} + r_3) = 2(r_{1,2})^2 / q_3 .$$

The explicit forms of the trigonal IP in terms of tensor elements become

$$q_{1,2} = 3kI_0[\tfrac{3}{4}(T_{11} + T_{22})^2 - T_{11}T_{22} + (T_{12})^2] ,$$

$$q_3 = 6kI_0(T_{33})^2 ,$$

$$r_{1,2} = 3kI_0[T_{11}T_{33} + T_{22}T_{33}] ,$$

$$r_3 = 3kI_0[\tfrac{1}{4}(T_{11} + T_{22})^2 + T_{11}T_{22} - (T_{12})^2] , \qquad (11)$$

$$s_{1,2} = 3kI_0[(T_{13})^2 + (T_{23})^2] ,$$

$$s_3 = 3kI_0[(T_{12})^2 + \tfrac{1}{4}(T_{11} - T_{22})^2] ,$$

$$t_1 = 3kI_0[T_{12}T_{13} + \tfrac{1}{2}(T_{11} - T_{22})T_{23}] .$$

The classification of 29 dynamical modes in 13 symmetries $O_1' \subset D_{3d}$ into 10 representative modes with 5 representative symmetries $O_1 \subset D_3$ and the correspondence to 8 different BT's for random distribution in trigonal crystals is given in Table III. The characteristic IP relations of these BT's are provided in Table IV.[27]

C. Comparison of discriminative power

In Table V we compare the capability of the BT method to distinguish dynamical modes Γ' and the symmetry O_1' of defects in different crystal systems on the basis of a BT analysis. The discriminative power quantified by figures reveals two general trends. (i) The variety of possible dynamical modes is reduced with decreased defect symmetry, because the defect symmetry is governed by the forces of the local crystal field. This means that the defect symmetry O_1' can only be a subgroup of the local symmetry of the site of defect incorporation, which in turn can only be a subgroup of the lattice symmetry G', i.e., $O_1' \subset G'$. Accordingly the numbers of representative modes and symmetries reduce when going from cubic to tetragonal and to trigonal crystals. (ii) The number of independent quantities, either IP's or polarized Raman intensities, increases when the symmetry of the environment decreases. This trend can be traced from the case of free molecules with two independent quantities to the three independent quantities $\{A_{1g}, E_g, T_{2g}\}$ or $\{q, r, s\}$ for *discrete* orientational distribution in cubic crystals.[30,31] The trend continues when the number of energetically equivalent orientations decreases. A similar effect is obtained when the high symmetry of random distribution $(F_1 = G)$ is lowered due to partial preferential orientation of the defects. For all three crystal symmetries, the number of distinguishable representative modes for the minimum orientational symmetry $F_1 = C_1$ is larger than for random distribution. The strongest enhancement occurs for cubic crystals as seen in the last two rows of Table V.

D. Measurement configurations

A complete test of the increasing number of BT relations in lower symmetric crystals requires the perfor-

TABLE III. Trigonal crystals. Classification of 29 dynamical modes Γ' in 13 symmetries $O_1' \subset D_{3d}$ according to 10 representative modes Γ into 5 representative symmetries $O_1 \subset D_3$.

Representative modes		Dynamical modes	
Representative symmetry	Representative mode	Number of modes	
C_1	A	2	$C_1{:}A \quad S_2{:}A_g$
$C_2[100]$	A	3	$C_2[100]{:}A \quad C_{1h}(100){:}A' \quad C_{2h}[100]{:}A_g$
	B	3	$C_2[100]{:}B \quad C_{1h}(100){:}A'' \quad C_{2h}[100]{:}B_g$
$C_2[1\sqrt{3}0]$	A	3	$C_2[1\sqrt{3}0]{:}A \quad C_{1h}(60°){:}A' \quad C_{2h}[1\sqrt{3}0]{:}A_g$
	B	3	$C_2[1\sqrt{3}0]{:}B \quad C_{1h}(60°){:}A'' \quad C_{2h}[1\sqrt{3}0]{:}B_g$
$C_3[001]$	A	2	$C_3[001]{:}A \quad S_6[001]{:}A_g$
	$E_{x'}$	2	$C_3[001]{:}E_{x'} \quad S_6[001]{:}E_g^{(1)}$
	$E_{y'}$	2	$C_3[001]{:}E_{y'} \quad S_6[001]{:}E_g^{(2)}$
$D_3[001]$	A_1	3	$D_3[001]{:}A_1 \quad D_{3d}[001]{:}A_{1g} \quad C_{3v}[001]{:}A_1$
	E	6	$D_3[001]{:}E_{x'}; E_{y'} \quad D_{3d}[001]{:}E_g^{(1)}; E^{(2)} \quad C_{3v}[001]{:}E_{x'}; E_{y'}$
$\Sigma = 5$	$\Sigma = 10$	$\Sigma = 29$	

TABLE IV. Listing of all BT's which can occur for random distribution in trigonal crystals, corresponding to the representative modes Γ and symmetries O_1 of Table III.

O_1	Γ	BT No.	IP relations							Additionally
C_1	A	BT 12	q_{12}	q_3	r_{12}	r_3	s_{12}	s_3	t_1	a
$C_2[100]$	A	BT 13a	q_{12}	q_3	r_{12}	r_3	s_{12}	s_3	t_1	a,b
	B	BT 24				r_3	s_{12}	$-r_3$	t_1	$r_3<0^b$
$C_2[1\sqrt{3}0]$	A	BT 13b	q_{12}	q_3	r_{12}	r_3	s_{12}	s_3	t_1	a,c
	B	BT 21	q_{12}			$-q_{12}$	s_{12}	q_{12}	t_1	d
$C_3[001]$	A	BT 25	q_{12}	q_3	r_{12}	q_1				e
	E_x	BT 19	q_{12}			$-q_{12}$	s_{12}	q_{12}	t_1	$t_1=-v_1,t_1\neq u_1$
	E_y	BT 17	q_{12}			r_3	s_{12}	s_3	t_1	$(q_{12}-r_3)=2s_3$
$D_3[001]$	A	BT 25	q_{12}	q_3	r_{12}	q_1				e
	B	BT 21	q_{12}			$-q_{12}$	s_{12}	q_{12}	t_1	d

$^a(q_{12}+r_3)=(2r_{12}^2/q_3)$.
$^bt_1=+(s_1s_3)^{1/2}$.
$^ct_1=-(s_1s_3)^{1/2}$.
$^dt_1=(q_{12}s_{12})^{1/2}$.
$^er_{12}=(q_{12}q_3)^{1/2}$.

mance of a larger number of polarized scattering intensity measurements. Adopting the terminology of Ref. 22, a single configuration of the polarization vectors of the incident and scattered light, $(\vec{a},\vec{b})$, shall be called an optical geometry pair (OGP). The set of possible OGP's for a single orientation of a crystal with respect to the wave vectors of the incident and scattered light, $(\vec{k}_{\mathrm{in}},\vec{k}_{\mathrm{out}})$, is called the OGP set. For practical reasons only rectangular scattering configurations are considered.

From the principles of crystal optics[32] it follows that tetragonal and trigonal crystals become optically uniaxial and birefringent. Let the optical axis be the $z\|[001]$ direction of the orthogonal crystal frame of reference

(x,y,z). For any direction of $\vec{k}$ not along $[001]$ only the two states of ordinary $(o)(\vec{E}\perp\vec{k},\vec{E}\perp[001])$ and extraordinary (e) ($\vec{E}$ within the plane spanned by $\vec{k}$ and $[001]$) polarization are possible.

For an easy determination of the IP's the OGP should be chosen, such that according to Eq. (5) the polarized intensities $I_{\vec{a},\vec{b}}$ become very simple linear expressions of the IP's. This is achieved when $\vec{a}$ and $\vec{b}$ are chosen along the orthogonal crystal axes $(x\|[100],y\|[010],z\|[001])$ or along the bisectors $(xy\|[110],x\bar{y}\|[1\bar{1}00]$, etc.).

A summary of suitable OGP sets is sketched in Fig. 1 as a guideline for the experimenter. The orientation of the crystal axes (x,y,z) is indicated for various crystal

TABLE V. Comparison of the discriminative power of the behavior-type method in cubic (Refs. 22 and 23), tetragonal (Ref. 24), and trigonal (Ref. 26) crystal symmetries.

|	Cubic	Crystal symmetry Tetragonal	Trigonal
Symmetry groups G,G'	O,O_h	D_4,D_{4d}	D_3,D_{3d}
Order h of G	24	8	6
Number of dynamical modes	124	80	29
in point groups $O_1'\in G'$	33	25	13
Classification according to			
representative modes	24	20	10
representative symmetries	10	8	5
Number of different BT's	65	46	25
IP's different from zero for $F_1=G$	3	6	7
independent IP's for $F_1=G$	3	5	6
Number of distinguishable representative modes for single mode BT analysis			
(a) for $F_1=G$	7	13	8
(b) for $F_1=C_1$	15	16	10
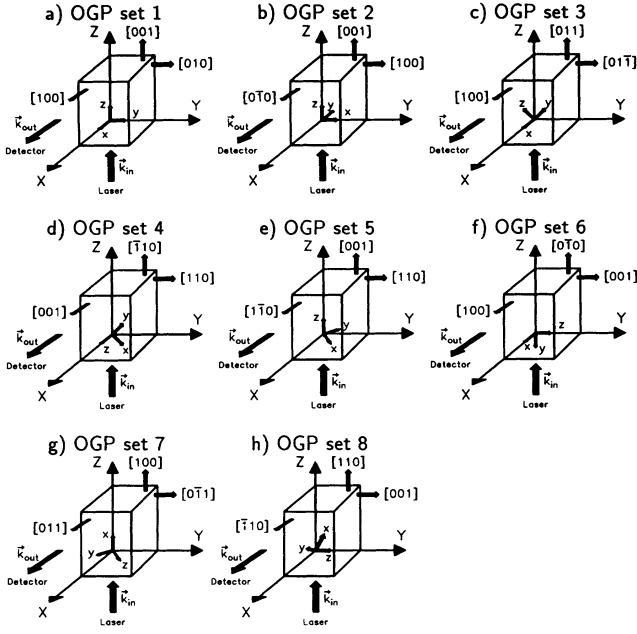
FIG. 1. Schematic sketch of the scattering configurations in the OGP sets 1–8 of Table VI.

orientations in the fixed laboratory frame of reference (X, Y, Z). This is defined by the incident laser beam $(\vec{k}_{in} \| Z)$ and the optical axis of the detection system $(\vec{k}_{out} \| X)$. In Table VI we summarize the explicit expressions for the polarized intensities $I_{\vec{a}, \vec{b}}$ in terms of the IP's calculated from Eq. (5) for the general case $F_1 = C_1$. The relations of the minimum BT, namely, Eqs. (7), (8), and (10), for cubic, tetragonal, and trigonal systems, respectively, can be applied to simplify the expressions.

The OGP sets 1–3 recommended in Ref. 22 suffice for cubic crystals. But the constraints of birefringence, which lower the number of OGP's per OGP set, and the need for additional OGP's due to the increased number of independent IP's in lower symmetric crystals, necessitate measurements in the OPG sets 4–6. These six OGP sets allow the determination of all the independent IP's, even for trigonal systems. OGP sets 7 and 8 yield redundant OGP's only. However, they may become useful when additional experimental constraints arise for specific materials; see Secs. IV B and IV C.

Polarized intensities $I_{\vec{a}, \vec{b}}$, obtained with different OGP sets, must be linked, because the detection efficiency k is very sensitive to experimental conditions. Therefore the same intensity $I_{\vec{a}, \vec{b}}$ has to be measured in two different OGP sets. Finally, the prescriptions to calculate the IP's from the intensities $I_{\vec{a}, \vec{b}}$ shall be given. From the expressions of Table VI using the minimum BT relations, Eqs. (7), (8), and (10), one finds

$$q_1 \propto I_{x,x}, q_2 \propto I_{y,y}, q_3 \propto I_{z,z} \ ,$$

$$s_1 \propto I_{y,z}, s_2 \propto I_{x,z}, s_3 \propto I_{x,y} \ , \tag{12}$$

$$(r_3 + s_3) \propto (I_{xy,xy} - I_{x\bar{y},xy}) \ .$$

The polarization vectors $\vec{a}$ and $\vec{b}$ may be interchanged in the $I_{\vec{a}, \vec{b}}$. The IP's t_1, v_1, and u_1 become relevant only for trigonal crystals. They can only be obtained by combining intensities measured in more than one OGP set.

A precise orientation of the crystal axes with respect to the laboratory frame of reference is very important. A complete theoretical description of the problem is given in Sec. III E of Ref. 22. Let β_i $(i = x, y, z)$ denote small angular deviations of the crystal axes with respect to the laboratory frame for rotations around the i axis. Then two cases can be distinguished for the dependence of the error ΔI of a polarized intensity. Either ΔI is of first order in β_i, i.e., $\Delta I \propto \beta_i$, or of second order, i.e., $\Delta I \propto \beta_i^2$ or $\Delta I \propto \beta_i \beta_j$. For precise intensity measurements the latter case is less critical. A calculation of the behavior of ΔI for the OGP's of OGP sets 1–8 has been performed for the case of random orientational defect distribution. The results can be summarized by stating that fortunately for nearly all OGP's ΔI is of second order in the β_i. The only exceptions are the OGP's of the type $(\vec{a}, \vec{b}) = (\rho, \rho\sigma)$ and $(\rho, \rho\bar{\sigma})$, where $(\rho, \sigma = x, y, z)$. For these OGP's the intensity takes the form $I_{\vec{a}, \vec{b}} \propto \frac{1}{2}(q_i + s_j \pm v_k)$; see Table VI. This means that the determination of the IP v_k $(k = 1, \ldots, 6)$ is very sensitive to angular deviations. In particular, this becomes relevant for trigonal systems, as the corresponding BT's involve relations with the IP $v_1 = -t_1$; compare Eq. (10) and Table IV.

III. EXPERIMENTAL DETAILS

A. Sample preparation

The samples were cut from boules of $SrTiO_3$, $KTaO_3$, $K_{1-x}Li_xTaO_3$ $(x = 0.022)$, TiO_2, and $LiTaO_3$ single crystals. An angular accuracy of better than $1°$ was guaranteed for the orientation of the sample surfaces. All six faces of the rectangular-shaped samples were grinded and polished to optical quality. This was essential for the suppression of stray light for the measurement of the very low scattering intensities of the OH stretch mode.

Without additional experimental constraints all necessary OGP sets can be performed for uniaxial crystals with *one* suitable shaped single crystal. The shape, the orientation, and the directions $\vec{k}_{in}(n), \vec{k}_{out}(n)$ of such a sample, which is suitable to realize the OGP sets n $(n = 1, \ldots, 8)$, are illustrated in Fig. 2. Starting from
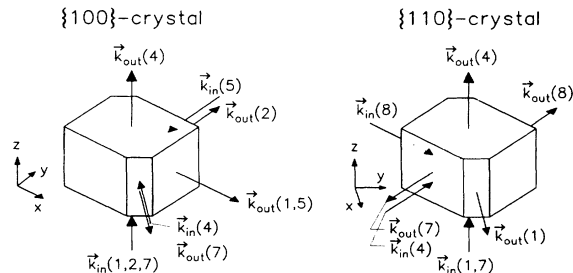

FIG. 2. Realization of the independent OGP sets 1, 2, 4, 5, and 7 from Table VI with one suitably prepared {100} crystal (left side). Realization of OGP sets 1, 4, 7, and 8 with one {110} crystal (right side).

TABLE VI. Polarized Raman scattering intensities $I_{\vec{a},\vec{b}}$, which can be measured in the OGP sets of Fig. 1, expressed as linear combinations of the IP's. An OGP $(\vec{a},\vec{b})$ in a certain OGP set generated by $\vec{k}_{in}$ and $\vec{k}_{out}$ is specified by using the Porto notation $\vec{k}_{in}(\vec{a},\vec{b})\vec{k}_{out}$. The OGP's are given in the crystal (x,y,z) frame and in the laboratory frame (X,Y,Z), where $Z\|\vec{k}_{in}, X\|\vec{k}_{out}$.

Lab. frame	Crystal frame	$I_{\vec{a},\vec{b}}$
	(a) OGP set 1: $\vec{k}_{in}\|z, \vec{k}_{out}\|x$	
$Z(Y,Y)X$	$z(y,y)x$	q_2
(Y,Z)	(y,z)	s_1
(X,Z)	(x,z)	s_2
(X,Y)	(x,y)	s_3
(XY,Y)	(xy,y)	$\frac{1}{2}(q_2+s_3+2v_6)$
$(X\bar{Y},Y)$	$(x\bar{y},y)$	$\frac{1}{2}(q_2+s_3-2v_6)$
(XY,Z)	(xy,z)	$\frac{1}{2}(s_1+s_2+2t_3)$
$(X\bar{Y},Z)$	$(x\bar{y},z)$	$\frac{1}{2}(s_1+s_2-2t_3)$
	(b) OGP set 2: $\vec{k}_{in}\|z, \vec{k}_{out}\|y$	
$Z(Y,Y)X$	$z(x,x)y$	q_1
(Y,Z)	(x,z)	s_2
(X,Z)	(y,z)	s_1
(X,Y)	(y,x)	s_3
(XY,Y)	$(x\bar{y},x)$	$\frac{1}{2}(q_1+s_3-2v_5)$
$(X\bar{Y},Y)$	(xy,x)	$\frac{1}{2}(q_1+s_3+2v_5)$
(XY,Z)	$(x\bar{y},z)$	$\frac{1}{2}(s_1+s_2-2t_3)$
$(X\bar{Y},Z)$	(xy,z)	$\frac{1}{2}(s_1+s_2+2t_3)$
	(c) OGP set 3: $\vec{k}_{in}\|yz, \vec{k}_{out}\|x$	
$Z(Y,Y\bar{Z})X$	$yz(y\bar{z},z)x$	$\frac{1}{2}(q_3+s_1-2v_2)$
(Y,YZ)	$(y\bar{z},y)$	$\frac{1}{2}(q_2+s_1-2v_1)$
$(X,Y\bar{Z})$	(x,z)	s_2
(X,YZ)	(x,y)	s_3
	(d) OGP set 4: $\vec{k}_{in}\|\bar{x}y, \vec{k}_{out}\|z$	
$Z(Y,Y)X$	$\bar{x}y(xy,xy)z$	$\frac{1}{4}(q_1+q_2)+\frac{1}{2}r_3+s_3+(v_5+v_6)$
(Y,Z)	$(xy,\bar{x}y)$	$\frac{1}{4}(q_1+q_2)-\frac{1}{2}r_3$
(Y,YZ)	(xy,y)	$\frac{1}{2}(q_2+s_3+2v_6)$
$(Y,Y\bar{Z})$	(xy,x)	$\frac{1}{2}(q_1+s_3+2v_5)$
$Z(X,Y)X$	(z,xy)	$\frac{1}{2}(s_1+s_2+2t_3)$
(X,Z)	$(z,\bar{x}y)$	$\frac{1}{2}(s_1+s_2-2t_3)$
(X,YZ)	(z,y)	s_1
$(X,Y\bar{Z})$	(z,x)	s_2
	(e) OGP set 5: $\vec{k}_{in}\|\bar{y}, \vec{k}_{out}\|x$	
$Z(Y,Y)X$	$\bar{y}(z,z)x$	q_3
(Y,Z)	(z,y)	s_1
(X,Y)	(x,z)	s_2
(X,Z)	(x,y)	s_3
	(f) OGP set 6: $\vec{k}_{in}\|x, \vec{k}_{out}\|yz$	
$Z(XY,Y)X$	$x(z,y\bar{z})yz$	$\frac{1}{2}(q_3+s_1+2v_2)$
(XY,Z)	(z,x)	s_2
$(X\bar{Y},Y)$	$(y,y\bar{z})$	$\frac{1}{2}(q_2+s_1-2v_1)$
$(X\bar{Y},Z)$	(y,x)	s_3
	(a) OGP set 7: $\vec{k}_{in}\|z, \vec{k}_{out}\|x\bar{y}$	
$Z(X,Y)X$	$z(x\bar{y},xy)x\bar{y}$	$\frac{1}{4}(q_1+q_2)-\frac{1}{2}r_3$
(X,Z)	$(x\bar{y},z)$	$\frac{1}{2}(s_1+s_2-2t_3)$
(Y,Y)	(xy,xy)	$\frac{1}{4}(q_1+q_2)+\frac{1}{2}r_3+s_3+(v_5+v_6)$

TABLE VI. (Continued).

Lab. frame	Crystal frame	$I_{\vec{a},\vec{b}}$
(Y,Z)	(xy,z)	$\frac{1}{2}(s_1+s_2+2t_3)$
(XY,Y)	(x,xy)	$\frac{1}{2}(q_1+s_3+2v_5)$
(XY,Z)	(x,z)	s_2
$(X\bar{Y},Y)$	(y,xy)	$\frac{1}{2}(q_2+s_3+2v_6)$
$(X\bar{Y},Z)$	(y,z)	s_1
	(a) OGP set 8: $\vec{k}_{in}\|xy, \vec{k}_{out}\|\bar{x}y$	
$Z(X,Y)X$	$xy(x\bar{y},z)x\bar{y}$	$\frac{1}{2}(s_1+s_2-2t_3)$
(X,Z)	$(x\bar{y},xy)$	$\frac{1}{4}(q_1+q_2)-\frac{1}{2}r_3$
(Y,Y)	(z,z)	q_3
(Y,Z)	(z,xy)	$\frac{1}{2}(s_1+s_2+2t_3)$

a cubic-shaped sample with 3–8 mm edges and (001), (010), and (100) faces, one grinds and polishes two opposite edges parallel to [001], such that additional narrow surfaces with [110] normals under 45° to the front faces of about 1–3 mm width will result. The OGP sets 1, 2, 4, 5, and 7 of Table VI can be realized with this specimen. Starting from a sample with (001), (110), and ($1\bar{1}0$) front faces and two opposite narrow (100) surfaces parallel to [001], one can realize the OGP sets 1, 4, 7, and 8.

In order to raise the expected very low scattering intensities we increased the hydrogen defect concentration c_H using the electric-field-enhanced in-diffusion of hydrogen from humid atmosphere[34] and/or a hydrothermal treatment similar to that described in Ref. 35. Because the in-diffusion technique produces an inhomogeneous hydrogen distribution, we concentrated on the hydrothermal treatment. Compared to the usual "as-grown" concentration we enhanced the concentration in $KTaO_3$ by a factor of 2, in $LiTaO_3$ by 4, in $SrTiO_3$ and in stoichiometric $LiNbO_3$ by 5, and finally in congruent $LiNbO_3$ by 90. Both the increase of c_H and the homogeneous distribution have been confirmed by monitoring the OH stretch mode absorption band.

B. Measurement of polarized intensities

In our experiments we used an Ar ion laser beam to excite the Raman scattering. The rectangular scattered light was imaged onto the entrance slit of a 0.75 m Czerny-Turner double monochromator. The conventional photon counting technique was used to detect the scattered intensity. The incident laser beam was repolarized with a fixed prism polarizer. Then it passed a rotatable $\lambda/2$ plate to define the incident polarization $\vec{a}=\hat{E}_{in}$ with constant intensity I_0. Using the same principle, the scattered light passed a polarizer to define $\vec{b}=\hat{E}_{out}$, which was followed by a $\lambda/2$ plate. This allowed us to rotate the polarization to the direction of maximum transmittance of the monochromator. Thus we eliminated the polarization dependence of the detection efficiency k.

Typical excitation conditions were $I_0=4-6$ W at 488 or 514 nm. For $SrTiO_3$ and $KTaO_3$ the OH bandwidth varied between $\Gamma\approx0.5$ cm^{-1} at $T=25$ K and $\Gamma\approx3.5$ cm^{-1} at room temperature. The corresponding data for TiO_2 and $LiTaO_3$ are 20 and 34 cm^{-1}, respectively. For $\Delta\bar{v}=1.5$ cm^{-1} the typical scattering intensities fell in the range of 70 ($SrTiO_3$) to 200 counts/s ($KTaO_3$) in OGP with $\vec{a}\|\vec{b}$, but only 4–15 % of this for configurations with $\vec{a}\perp\vec{b}$.

For the BT analysis of a mode, the relevant symmetry information is contained only in the ratios of the polarized intensities $I_{\vec{a},\vec{b}}$. Once it was proved that the spectral distribution of the OH band of a crystal material does not depend on the OGP $(\vec{a},\vec{b})$, we used a spectral window technique for faster and/or more precise measurements. The spectral resolution $\Delta\bar{v}$ was set to approximately 1.3 times the value of the bandwidth Γ. With the center of a spectral window at the maximum of the spectral distribution we performed an integration of the peak intensity. The contribution of the background was determined at two frequencies symmetrically left and right outside of the OH band and then substracted. Using the window technique we obtained an accuracy as good as 3% for intensity ratios measured in the same OGP set.

The long term stability of the detection sensitivity was checked periodically by measuring the Raman intensities of prominent and spectrally isolated lines of the phonon spectrum. In addition to the redundant measurement of specific IP's of the OH band in different OGP sets $(\vec{k}_{in},\vec{k}_{out})$ the off-diagonal Raman tensor elements of such lattice mode intensities were also used to link the OH intensities in different OGP sets. In the case of TiO_2, this was the only procedure left, because the IP's s_1 and s_2 of the OH band otherwise used for linking were equal to zero.

Apart from the statistical uncertainties due to low scattering intensities, a more important source of systematic experimental errors is the misalignment of the crystal axes (x,y,z) with respect to the rectangular laboratory frame (X,Y,Z), defined by $\vec{k}_{in}\|Z$ and $\vec{k}_{out}\|X$. In the course of our investigations we have developed a practical experimental procedure to realize precise alignment of these axes.[33,36]

IV. RESULTS AND DISCUSSION

A. Hydrogen in perovskite crystals

Elaborate investigations have been performed, including measurements of the temperature dependence,[15,17,18] in combination with electric[15,19] or uniaxial stress[19] fields and the effects of H-D substitution[16,19,4] on the OH absorption. Still two contradicting models for the hydrogen sites are controversially discussed.[19,20] The present Raman investigations were intended to solve this conflict by considering the local symmetry properties of the OH stretch mode.

The perovskite crystal structure is cubic primitive; the crystal point group G' is $O_h(m\bar{3}m)$. The ions of the basis occupy the following sites: A is located at $(0,0,0)$, B at $(\frac{1}{2},\frac{1}{2},\frac{1}{2})$, and O^{2-} at $(\frac{1}{2},\frac{1}{2},0)$, $(\frac{1}{2},0,\frac{1}{2})$, $(0,\frac{1}{2},\frac{1}{2})$. In Fig. 3 we illustrate the three models introduced for hydrogen sites. An arbitrary initial orientation v_1 of the OH dipole and the symmetry elements of the point group O'_1, which describe the local symmetry of the defect, are sketched for each model in the cubic unit cell. The protons are bound on interstitial sites close to O^{2-} ions. The resulting OH dipole is represented by a bold arrow. The $C_{\infty v}$ symmetry of the free OH dipole is reduced to the finite subgroup $O'_1 \subseteq G' \subset C_{\infty v}$. The energetically equivalent orientations $v_n = R_n v_1$ with $R_n \in G'$ will be found in different unit cells and within the scattering volume all these orientations will occur with a common average population number.

According to the *cube axis (CA) model*[18] the proton was believed to vibrate towards another oxygen ion in the direction of the cubic crystallographic axes, the next-nearest O^{2-} ion. This is located at a distance $R_{O-O} = a$, the lattice constant. One twofold axis $C_2[001]$ and two vertical mirror planes $\sigma(100)$ and $\sigma(010)$ are identified to define the local symmetry; thus $O'_1 = C_{2v}[100](100,010)$ and $O_1 = D_2[100]$ for the representative symmetry from Table I.

In the *octahedron edge (OE) model*,[16] the proton is believed to vibrate along an edge of the BO_6 octahedron towards the nearest-neighbor O^{2-} ion $(R_{O-O} = a/\sqrt{2})$. The OH dipole points along a $\langle 110 \rangle$-type direction. Only a $\sigma(010)$ mirror plane exists with a point group

$O'_1 = C_{1h}(010)$ represented by $O_1 = C_2[010]$; see again Table I.

In the *cube face (CF) model*,[17] the hydrogen is oriented along the face diagonal of the cubic unit cell towards the A cation. A twofold axis $C_2[\bar{1}01]$ and two vertical mirror planes $\sigma(010)$ and $\sigma(101)$ represent the local symmetry of such a site. Therefore $O'_1 = C_{2v}[\bar{1}01](101,010)$, which is represented by $O_1 = D_2[\bar{1}01] = D_2[110]$.

1. KTaO₃

Nominally pure $KTaO_3$ exhibits only one single absorption line even at $T = 1.5$ K. At room temperature the band maximum is observed at $\bar{v}_{max} = 3474$ cm^{-1} and the half width is $\Gamma = 3.8$ cm^{-1}. Upon cooling to $T = 1.5$ K the frequency increases continuously to 3488 cm^{-1} and the half width narrows to 0.3 cm^{-1},[37] reflecting the fact that pure $KTaO_3$ preserves its cubic symmetry.

For polarized Raman scattering in pure $KTaO_3$ we used the same crystal as in the ir investigations reported in Refs. 37 and 38. We measured the Raman spectra in Fig. 4 according to the OGP sets 1 and 7 of Table VI and determined the three independent IP's q, r, and s. The three peaks with weak intensity are clearly not related to OH defects. They are due to elastically scattered photons from plasma discharge transitions in Ar. These plasma lines were advantageously used as a reference for the frequency position of the OH bands and for the spectral resolution of the detection system. The latter is identical to the observed half width of a single plasma line.

The equality of the intensities $I_{y,z} \propto s_1$, $I_{x,z} \propto s_2$, and $I_{x,y} \propto s_3$ measured in OGP set 1 indicate that within experimental accuracy, the relation $s_1 = s_2 = s_3 \equiv s$ of the general BT's in cubic crystals [compare Eq. (7)] is satisfied.

According to Table VI the two equalities $I_{y,yz} = I_{y,y\bar{z}}$ and $I_{y,yz} = I_{y,\bar{y}z}$ indicate that the IP's $v_1 = 0$ and $v_6 = 0$, respectively. The sample was rotated by 90° about $\vec{k}_{in}$ and $\vec{k}_{out}$, in order to check in OGP sets 2 and 5 the relations $v_3 = v_5 = 0$ and $v_2 = v_4 = 0$, respectively, as well as the relation $q_1 = q_2 = q_3 \equiv q$ of the general BT, Eq. (7). For all crystals and all crystal symmetries investigated in this work we have performed similar tests of the minimum
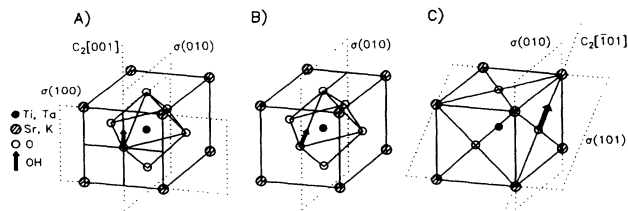

FIG. 3. Schematic representation of the three models for hydrogen incorporation in the perovskites, (a) the cube axis (CA) model, (b) the octahedron edge (OE) model, and (c) the cube face (CF) model, within the cubic unit cell. For each model the OH dipole is sketched only in an arbitrary initial orientation v_1, together with the elements of the point group O'_1 representing the local symmetry.
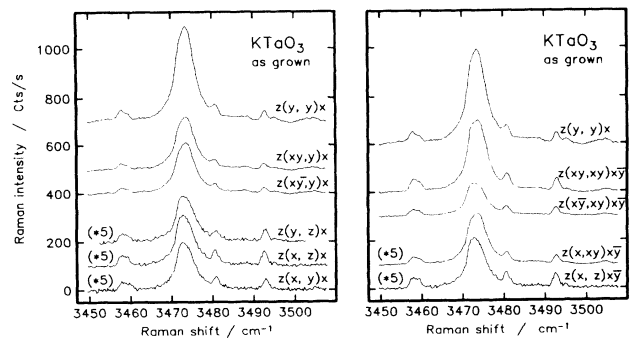

FIG. 4. Polarized Raman spectra of the OH stretch mode in a nominally pure $KTaO_3$ crystal, measured at room temperature in OGP set 1 (left part) and OGP set 7 (right part).

BT relations, Eqs. (7) for cubic, (8) for tetragonal, and (10) for trigonal crystals, in order to check the adjustment of the experimental setup and the polarization properties of the samples. In all conclusive experiments concerning the symmetry of the hydrogen sites, these relations proved to hold actually.

Conclusions concerning the local defect symmetry follow from the s/q and r/q ratios. The relevant intensity values were precisely measured using the spectral window technique and inserted into Eqs. (12) to calculate the IP's. Together with the IP's of the OH bands in other crystals, the r/q and s/q ratios are collected in Table VII.

In a BT analysis of the figures in Table VII it is important, first, that $q > 0$ hold. Thus the OH stretch mode is an A mode as expected, because in cubic crystals all other modes demand $q = 0$. From the set {BT 60, BT 50, BT 39, BT 13} belonging to A modes, the results $1 > r > 0$ and $s > 0$ uniquely select BT 60. The same BT 60 has been observed at room temperature for the 3474 cm^{-1} band in $K_{1-x}Li_xTaO_3$ samples with $x = 0.018$ and 0.023.

The Li-doped sample with $x = 0.018$ has been investigated before (as grown) and after a hydrothermal treatment (973 K, $p_{H_2O} = 4 \times 10^7$ Pa); see Fig. 5. The ir absorption constant and the Raman intensity of the 3474 cm^{-1} band increase by the same factor. The r/q and s/q ratios remain unaltered. However, the Raman spectrum of the hydrogen-doped sample exhibits an additional peak for $I_{y,y} \propto q$ at the high energy shoulder with a maximum at 3488 cm^{-1}. This peak cannot be identified in the corresponding ir absorption spectrum. The polarized Raman spectra of the H-doped $x = 0.018$ sample yield $I_{y,y} \propto q > 0$ and $1 > r > 0$. But in contrast to the behavior of the prominent band at 3474 cm^{-1} the intensities $I_{y,z} \propto s_1, I_{x,z} \propto s_2, I_{x,y} \propto s_3$ for the satellite peak at 3488 cm^{-1} are not detected, either because they are zero or because they are below the detection limit. Therefore, the vanishing of these IP's cannot definitely be ruled out.

In our BT analysis we identified a cubic BT 60 for the prominent band. This result shall be related to the three models in Fig. 3. For the CA model with $O_1 = D_2[100]$, one would expect the cubic BT 50. In particular, BT 50 requires $s/q = 0$, in obvious disagreement with the experimental result $s \neq 0$. For both of the other models sketched in Fig. 3, the OE ($O_1 = C_2[110]$) *and* the CF models ($O_1 = D_2[110]$), a BT 60 is expected and found.
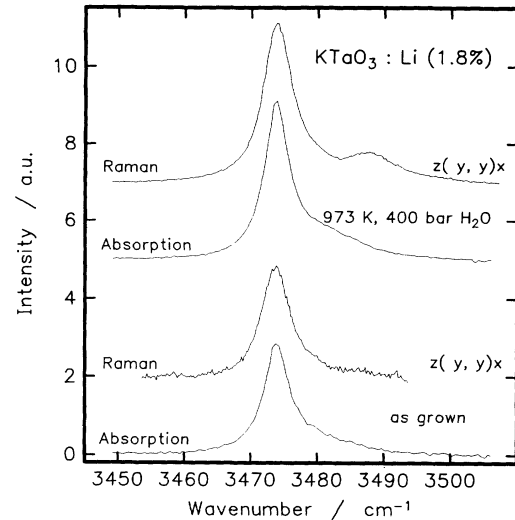

FIG. 5. Comparison of the Raman and ir absorption spectra of a $K_{1-x}Li_xTaO_3$ ($x = 0.018$) crystal, before (as grown) and after a hydrothermal proton doping (973 K, $p_{H_2O} = 4 \times 10^7$ Pa). All spectra were recorded at room temperature.

Consequently the CA model can definitely be ruled out for the main band in KTaO$_3$ and $K_{1-x}Li_xTaO_3$ already in the cubic phase.

Because of the many-to-one mapping of representative defect symmetries onto the BT's the other two models cannot be discriminated in the cubic phase. Moreover, any other site of incorporation of the proton, not described by the three models, is consistent with our Raman data. This is because such sites would be represented by $O_1 = C_1$ and would yield the observed BT 60, too. We point out that because of the isotropic behavior of the ensemble for all three models no discrimination is possible at all by means of ir absorption in cubic crystals.

2. Cubic SrTiO$_3$

The Raman spectra in the cubic phase of SrTiO$_3$ in Fig. 6 have been recorded with 514 nm excitation at room temperature in order to minimize spectral overlap with plasma lines. One plasma line now appears at 3478

TABLE VII. Summary of the IP ratios r/q and s/q of the OH stretch mode in various investigated cubic perovskite crystals.

Crystal	$\bar{\nu}/\text{cm}^{-1}$	r/q	s/q
KTaO$_3$ (pure)	3474	0.32±0.04	0.099±0.007
KTaO$_3$:Li (1.8%)	3474	0.73±0.07[a]	0.047±0.006[a]
KTaO$_3$:Li (2.3%)	3474	0.75±0.06	0.049±0.008
SrTiO$_3$	3496 (A)[b]	0.75±0.03[a]	0.049±0.008[a]
SrTiO$_3$:H[c]	3511 (C)[b]	0.205±0.020	0.070±0.009
	3515 (D)[b]	0.316±0.023	0.031±0.006
	3536 (F)[b]	0.128±0.019	0.022±0.010

[a]Before and after hydrothermal doping.
[b]Labeling according to Ref. 39.
[c]Hydrothermal doping 973 K, $p_{H_2O} = 4 \times 10^7$ Pa.
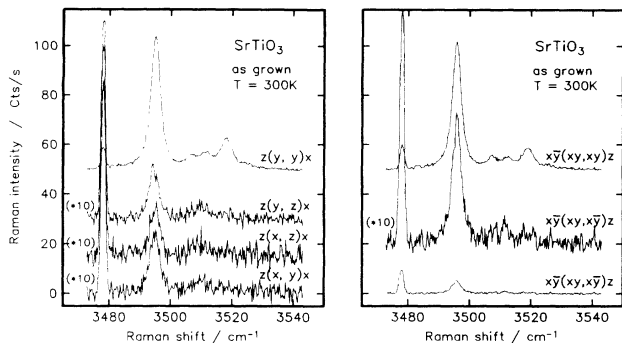
FIG. 6. Polarized Raman spectra of the OH stretch mode in SrTiO₃, measured at room temperature in OGP sets 1 (left part) and 4 (right part).

cm^{-1}. The main OH band is found at 3496 cm^{-1}. The structures in Fig. 6 above 3500 cm^{-1} belong to Fe-associated OH complexes discussed later. We concentrate on the 3496 cm^{-1} line caused by undisturbed protons. From OGP set 1 in the left part of Fig. 6 we find the relation $s_1 = s_2 = s_3 \equiv s \neq 0$. The analog relation is observed for the IP's $q_1 = q_2 = q_3 \equiv q \neq 0$. From the right part of Fig. 6 we read $1 > r/q > 0$. As for the main band in KTaO₃ a cubic BT 60 is also identified in SrTiO₃.

A strong hydrothermal treatment (973 K, $p_{H_2O} = 4 \times 10^7$ Pa) gave rise to additional, strong, high frequency OH bands. The new bands were attributed by Waser[13] to associate complexes of OH defects with Fe impurities in the crystals. The ir and Raman spectra are shown in Fig. 7. The bands labeled B and E in Fig. 7 do not appear in the Raman spectrum and the relative intensities of the other bands differ considerably from the ir
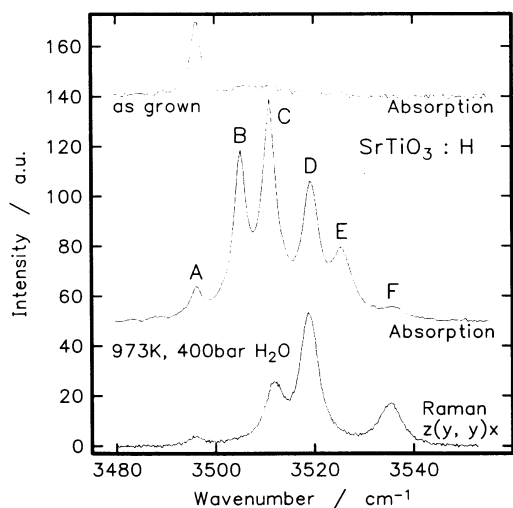
FIG. 7. Effect of the hydrothermal treatment (973 K, $p_{H_2O} = 4 \times 10^7$ Pa) on the OH spectrum of nominally pure SrTiO₃ due to Fe impurities. The ir absorption spectra before (upper curve) and after (central curve) doping are compared with the Raman spectrum after doping (bottom curve).

absorption spectrum. Similar to the main OH band labeled A, the Fe-associated bands C, D, and F exhibit the cubic BT 60. In addition we obtained $s_1 = s_2 = s_3 \equiv s \neq 0$ and the relation $1 > r/q > 0$. While obeying BT 60 all the OH bands in SrTiO₃ exhibit different r/q and s/q ratios. The precise values are summarized in Table VII. The discussion of the behavior of the main band in SrTiO₃ follows precisely the route for the main band in KTaO₃. The result $s \neq 0$ (BT 60) again rules out the CA model. Because all Fe-associated sidebands exhibit BT 60, they are of no use for a model distinction.

B. Tetragonal SrTiO₃

The CA model has already been ruled out. Although the three models of Fig. 3 differ with respect to the representative symmetry, the OE and the CF models induce the same cubic BT and have no distinguishing feature. With a partial preferential orientation of the defects there exist a distinct possibility. Indeed an inspection of Table VIII from Ref. 22 reveals that the cubic BT's for the OE and the CF models differ in lower symmetry of random distribution. However, to the best of our knowledge no traces of reorientation of OH defects in oxide materials have been observed until now. Instead we make use of the increase of the discriminative power of the BT method in lower symmetric hosts. We analyze the influence of the tetragonal crystal structure on the local symmetry of the OH defect.

The structural cubic-to-tetragonal phase transition in SrTiO₃ at $T_c \approx 105$ K is described by a counterwise rotation of the oxygen octahedra around one of the former cubic axes, reducing the symmetry to the point group $D_{4h}(4/mmm)$.[40] This leads to an unpolar, antiferrodistortive, tetragonal phase; see Fig. 8. Because no preferential direction exists for the rotation of the octahedra, uniaxial stress $\vec{S}$ is used while cooling the crystal below T_c to align the axes of the domains perpendicular to $\vec{S}$. The alignment is preserved, even with $\vec{S}$ removed. Practically monodomain crystals with their tetragonal axis $z \parallel [001]$ are obtained when a pressure $S_{110} > 55$ N/mm² is applied along the [110] direction.[41] The tilting angle is $\varphi = 2.1°$ at $T = 4.2$ K.[42]
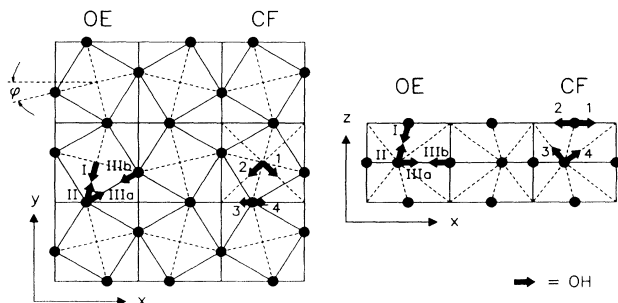

FIG. 8. Schematic sketch of the antiferrodistortive structure of the tetragonal phase of SrTiO₃. The left part shows a projection in the x-y plane, the right part in the x-z plane. The hydrogen sites according to the OE and the CF models are indicated in both projections.

The structural changes induce a temperature-dependent splitting of the OH band into three components $v_A < v_B < v_C$.[15] These features are also observed in the Raman spectra. Polarized absorption in mono-domain samples[19] shows that the central line v_B is polarized perpendicular to the tetragonal (z) axis. Therefore v_B is associated to sites, where the OH dipole is oriented within the xy plane. The outer two components v_A and v_C possess equal polarization components parallel and perpendicular to z. This indicates an angle of 45° with respect to the z axis.

In Fig. 9 we have sketched the energetically different sites of hydrogen for the two competing models. The labeling was taken from Refs. 19 and 20. According to the CF model the central line v_B is attributed to the ensemble of eight equivalent sites generated by the two representative sites 1 and 2, while in the OE model v_B is attributed to the ensemble generated by the sites labeled IIIa and IIIb. An assignment of the outer two lines v_A and v_C to one of the ensembles generated by sites 3 and 4 of the CF model has not been claimed.[20] The assignment of v_A to ensemble II and v_C to ensemble I in the framework of the OE model is not stringent.

Both models have their drawbacks (for details see Refs. 19 and 20) and both can principally not be distinguished by ir absorption. Even from electric-field-induced line splitting patterns and from polarized absorption one can only deduce information on the direction cosines of the dipole moment $\vec{p}_{OH}$. For each of the dipole ensembles I, II, or {IIIa,IIIb}, in the OE model there is a corresponding ensemble 3, 4, or {1,2} in the CF model, respectively, with the same direction of the dipole.

We start the discussion of the predictions of the BT theory in tetragonal systems with a recapitulation of the local symmetry elements in the cubic phase. In the CF model there are a diagonal twofold axis $C_2[\bar{1}01]$ and two vertical mirror planes $\sigma(010)$ and $\sigma(101)$, or equivalents for the other sites, while in the OE model there is only one mirror plane $\sigma(010)$, or equivalents (Fig. 9). Unfortunately, the different symmetry groups $O_1'(CF) = C_{2v}[110]$ and $O_1'(OE) = C_{1h}[010]$ lead to the same BT's in cubic crystals. In the tetragonal phase the situation becomes more complicated, but more favorable.[21,43]

First we concentrate on the sites of the CF model. Be-

cause of the tilting of the octahedra, only one symmetry element is preserved for each site, namely, $\sigma(010)$ for sites 3 and 4, and $\sigma(001)$ for sites 1 and 2. This is because during the rotation of the octahedra sites 3 and 4 remain within the vertical $\sigma(010)$ mirror plane, although leaving the center of the square; see Fig. 8. Hence for the outer two lines v_A and v_C (site 3 or 4) the local symmetry is $O_1'(CF,v_A) = O_1'(CF,v_C) = C_{1h}(010)$ and for the central line v_B (sites 1,2) it is $O_1'(CF,v_B) = C_{1h}(001)$. From Table VI in Ref. 24 we read the representative symmetries $O_1(CF,v_A) = O_1(CF,v_C) = C_2[010]$ and $O_1(CF,v_B) = C_2[001]$, for which according to Table II the tetragonal BT 24 and BT 26 are expected, respectively.

Now we consider the situation for the OE model. Upon rotation of the octahedron sites I and II move out of the vertical mirror plane $\sigma(010)$ (see Fig. 9), while the corresponding horizontal mirror plane $\sigma(001)$ of sites IIIa and IIIb is preserved; see Fig. 8. The resulting local symmetries of the sites are $O_1'(OE,v_A) = O_1'(OE,v_C) = C_1$ and $O_1'(OE,v_B) = C_{1h}(001)$. According to Table VI in Ref. 24 these correspond to the representative symmetries $O_1(OE,v_A) = O_1(OE,v_C) = C_1$ and $O_1(OE,v_B) = C_2[001]$, which are related to the tetragonal BT 21 and BT 26, respectively, see Table II.

Comparing the predictions of both models we note that the symmetry $O_1' = C_{1h}(001)$ and therefore the tetragonal BT 26 for the central line v_B is equal for both models. The BT's for v_A, v_C in the CF model and for v_A, v_C in the OE model differ in the IP s_3:[43] According to the OE model, $O_1'(OE) = C_1$, one expects a nonzero intensity $I_{x,y} \propto s_3 \neq 0$ (BT 21), while the existence of the vertical mirror plane $\sigma(010)$ in the CF model, $O_1'(CF) = C_{1h}(010)$, forces this IP to be zero, $s_3 = 0$ (BT 24). Thus a discrimination between the two models is only possible via the BT's of the outer two components v_A and v_C.

In Ref. 43 we suggested the only possible experiment to test this difference. It is read from Table VI that even under the constraints of birefringence the intensity $I_{x,y} \propto s_3$, i.e., and OGP with $(\vec{a},\vec{b}) = (x,y)$, can in principle be realized in any of the OGP sets 1, 2, 3, 5, or 6. However, additional constraints arise because of the need to apply uniaxial stress $\vec{S} \| [110]$ to obtain monodomain crystals. This required the preparation of an unusual octagon-shaped crystal for our investigations and an arrangement like that sketched in Fig. 3 of Ref. 43. Such an arrangement corresponds to OGP set 1 of Table VI.

The crystal was slowly cooled below T_c in a liquid He cryostat (0.5 K/min) while applying the $\vec{S}_{110}$ uniaxial pressure. At $T = 50$ K well below T_c the pressure was removed. From a measurement of all the independent tetragonal IP's of the OGP sets 7 and 8 it was possible to reconstruct the Raman tensor of a single defect.

The temperature dependence of the intensities $I_{y,y} \propto q_{1,2}$ and $I_{z,z} \propto q_3$, integrated over all the three well-resolved subbands, shows a steady increase upon lowering the temperature, apart from a significant dip at T_c. One cannot distinguish whether the dip is due to a lowered detection efficiency as a consequence of refractive index fluctuations or critical opalescence near T_c or
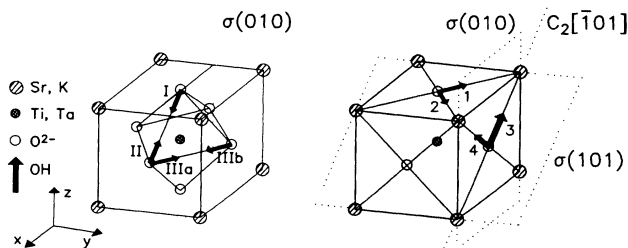

FIG. 9. Schematic sketch of the energetically different sites of hydrogen according to the OE (left part) and the CF (right part) models in the *tetragonal phase* of SrTiO$_3$. The symmetry elements, which are remanent from the *cubic phase*, are indicated for the sites related to the outer two components v_A and v_C.

another physical effect, which affects the polarizability changes $\partial \alpha / \partial Q$ of the OH stretch mode. The steady increase can be understood by assuming that the polarizability changes of the electronic charge distribution of the OH bond are attenuated by the lattice vibrations. This unexpected effect facilitated the precise measurement of the low intensities for the BT analysis, especially in the discriminating OGP's with $\vec{d} \perp \vec{b}$.

The polarized spectra of Fig. 10 form the basis of the BT analysis of v_A, v_B, and v_C. The tetragonal IP's for the individual subbands calculated from the polarized intensities $I_{\vec{a},\vec{b}}$ of Fig. 10 are summarized in Table VIII. The relevant characteristic IP relations can directly be read from the spectra. For the central band v_B the IP $s_{1,2} \propto I_{x,z}$ vanishes, while $s_3 \propto I_{x,y}$ is different from zero. For the outer bands v_A and v_C it is found that $s_1 = s_2 \neq 0$ and $s_3 \neq 0$. That is, all three IP's s_i ($i = 1,2,3$) are different from zero. The other tetragonal IP's $q_{1,2}$, q_3, and r_3 all are independent in the sense of the BT relations given in Table II. Therefore we clearly determined the tetragonal BT 21 for the outer bands v_A and v_C and BT 26 for the central band v_B.

It will turn out in the following discussion that especially the existence or nonexistence of reflection symmetries lead to discriminating model decisions. In Table IX we therefore combine Table VI in Ref. 24 and Table II and display a useful extraction. The inspection of this table reveals a direct correspondence between individual mirror symmetries and related IP relations.

First we consider the central band v_B. The tetragonal BT 26 is related to the representative symmetry $O_1 = C_2[001]$; see Table II. One of the corresponding actual symmetries in Table VI of Ref. 24 is $O_1' = C_{1h}(001)$. The horizontal mirror plane $\sigma(001)$ is compatible to the predictions of both, the OE (for sites IIIa and IIIb) and the CF model (for sites 1 and 2 indicated in Fig. 9). The existence of the $\sigma(001)$ mirror plane is the Raman analog to the ir dichroism polarized perpendicular to the [001] axis. According to Table IX one can say that the horizontal mirror plane $\sigma(001)$ induces the IP $s_{1,2}$ to be zero. This is exactly our interpretation of the behavior of $s_{1,2}$ for v_B.

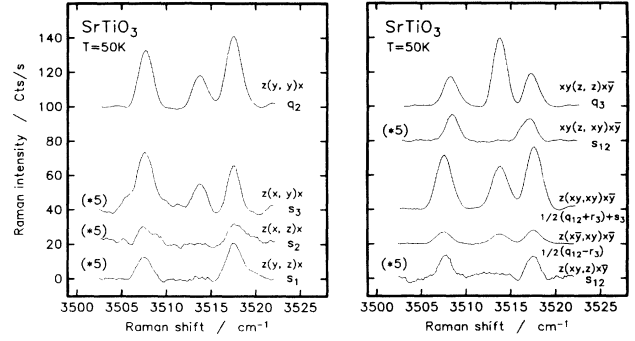The vanishing of $s_{1,2}$ for v_B ensures that the crystal was actually monodomain during the experiment. There-

FIG. 10. Polarized Raman spectra of the OH stretch mode in the tetragonal phase of $SrTiO_3$ recorded at $T = 50$ K. Left part: intensities measured to determine the IP's $q_{1,2}$, s_1, s_2, and s_3 from the OGP set 1. Right part: intensities measured to determine r_3 and q_3 from OGP sets 7 and 8, respectively.

fore the nonzero intensity $I_{x,y} \propto s_3$ is not a contribution from polydomain regions in the crystal. Furthermore, from the fact that the intensity ratios $I_{y,y} \propto q_{1,2}$ and $I_{x,y} \propto s_3$ for the outer lines v_A and v_C are different, we can rule out that the nonzero IP s_3 is a remanent of the intense IP $q_{1,2}$.

Now we consider the outer bands v_A and v_C. The CF model predicts the existence of a vertical mirror plane $\sigma(010)$ for the related sites 3 or 4. From Table IX we note that this would induce the vanishing of the IP s_3. This clearly contradicts the experimental result, $s_3(v_A) \neq 0 \neq s_3(v_C)$. Thus the nonvanishing of the IP s_3 rules out the validity of the CF model and the existence of a vertical mirror plane $\sigma(010)$.[21]

Because of the observed BT 21, the local *symmetry* of the outer bands v_A and v_C is $O_1 = C_1$. From this result alone the *directions* of the dipoles are not at all determined. From the Raman data we only concluded the existence of a reflection symmetry for the sites related to v_B. In principle this still allows for any OH dipole direction within the mirror plane. But the fact that the dipole axes make angles of 45° with the crystallographic axes determines the direction to be along the oxygen octahedron edge.

In addition to the model decision our Raman data al-

TABLE VIII. Summary of the IP's for the subbands v_A, v_B, v_C measured in tetragonal $SrTiO_3$ at $T = 50$ K. For each subband the IP's are normalized to $q_{1,2}$ in lines 4–8. In line 3 the IP's $q_{1,2}$ are normalized to the most intense subband v_C.

Line frequency	v_A/cm^{-1} 3507.8	v_B/cm^{-1} 3513.7	v_C/cm^{-1} 3517.3	Uncertainty[a]
$q_{12}/q_{12}(v_C)$	0.79±0.04	0.44±0.03	1.00	
q_{12}	1.000	1.000	1.000	
q_3	0.520±0.109	2.190±0.460	0.467±0.098	21%
r_3	0.517±0.068	0.859±0.118	0.548±0.071	13%
s_{12}	0.082±0.021	<0.02	0.082±0.021	25%
s_3	0.244±0.012	0.190±0.011	0.147±0.008	5%
BT_{tet}	21	26	21	

[a]For the normalization of the intensities $I_{\vec{a},\vec{b}}$ measured in different OGP sets.

TABLE IX. Summary of the possible actual symmetries O'_1 of the OH defect in the tetragonal crystals $SrTiO_3$, $KTaO_3$:Li, and TiO_2 considered in this work. This extract from Table VI in Ref. 24 and Table II gives a direct correspondence between specific (reflection) symmetries and the corresponding IP relations.

Local symmetry O'_1	BT_{tet}	IP relations						
C_1	21	$q_{1,2}$	q_3	$r_{1,2}$	r_3	$s_{1,2}$	s_3	a
$C_{1h}(010)$	24	$q_{1,2}$	q_3	$r_{1,2}$	r_3	$s_{1,2}$		a
$C_{1h}(001)$	26	$q_{1,2}$	q_3	$r_{1,2}$	r_3		s_3	a
$C_{1h}(110)$	22	$q_{1,2}$	q_3	$r_{1,2}$	$q_{1,2}$	$s_{1,2}$	s_3	a,b
$C_{2v}[1\bar{1}0](110,001)$	27	$q_{1,2}$	q_3	$r_{1,2}$	$q_{1,2}$		s_3	a,b

^{a}Additional IP relation $(q_{1,2}+r_3)=2(r_{1,2})^2/q_3$.
^{b}Additional IP relation $r_{1,2}=(q_{1,2}q_3)^{1/2}$.

low one to reconstruct the Raman tensors of the defects in their molecular frame. Based on the tentative assignment of v_A to site II, v_B to sites IIIa and IIIb, and v_C to site I of the OE model[19] we have sketched the representative OH defects together with their molecular frames in Fig. 11. For all sites the rectangular frames $(\tilde{x},\tilde{y},\tilde{z})$ are chosen such that $\tilde{z}$ is parallel to the OH dipole $\vec{p}_{OH}\|\tilde{z}$ and one other axis is oriented along a second octahedron edge. Then the third axis, perpendicular to both, points along one of the former cubic axes. Let these crystal axes $\vec{r}=(x,y,z)$ be defined by $x\|[100]$, $y\|[010]$, and $z\|[001]$. Then we have for the OH sites in Fig. 11

$$v_A(II): \begin{cases} \tilde{x}\|[100], \\ \tilde{y}\|[0\bar{1}1], \\ \tilde{z}\|[011], \end{cases} \quad v_B(III): \begin{cases} \tilde{x}\|[\bar{1}10], \\ \tilde{y}\|[001], \\ \tilde{z}\|[110], \end{cases} \quad v_C(I): \begin{cases} \tilde{x}\|[\bar{1}00], \\ \tilde{y}\|[01\bar{1}], \\ \tilde{z}\|[0\bar{1}\bar{1}]. \end{cases}$$

(13)

From these relations one can read the elements of the transformation matrices $\bar{R}$, which transform the crystal axes $\vec{r}$ to the molecular frame, $\vec{\tilde{r}}=\bar{R}\vec{r}$, and relate the Raman tensor $\bar{\bar{T}}^{(1)}$ in the crystal frame to the Raman tensor in the molecular frame $\bar{\bar{T}}$ according to

$$\bar{\bar{T}}^{(1)}=(\bar{R})^{-1}\bar{\bar{T}}\bar{R} .$$

(14)

We note that the elements of $\bar{\bar{T}}^{(1)}$ are obtained from the intensities $I_{\vec{a},\vec{b}}$ by the quadratic equation (9). Therefore,
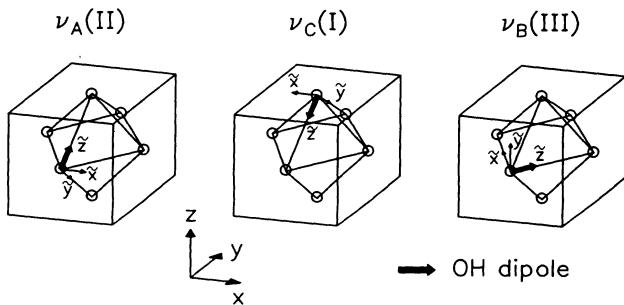

$$v_A(II) \qquad v_C(I) \qquad v_B(III)$$

FIG. 11. Schematic sketch of the OH dipoles and the molecular frames $(\tilde{x},\tilde{y},\tilde{z})$ used for the reconstruction of the Raman tensors in arbitrary initial orientations v_1 of the ensembles II, III, and I related to the subbands v_A, v_B, and v_C, respectively.

two solutions are obtained when setting $4kI_0=1$, viz.,

$$T_{11}=\pm\frac{1}{2}(\sqrt{q_1+r_3}+\sqrt{q_1-r_3}) ,$$

$$T_{22}=\pm\frac{1}{2}(\sqrt{q_1+r_3}-\sqrt{q_1-r_3}) ,$$

$$T_{11}=\pm\sqrt{\tfrac{1}{2}q_3} ,$$

(15)

$$T_{12}=\pm\sqrt{\tfrac{1}{2}s_3} ,$$

$$T_{13}^2+T_{23}^2=s_1 .$$

For the central band v_B we have four nonzero IP's, their number equaling the number μ_T of Raman tensor elements for an A' mode with $O'_1=C_{1h}(001)$; see Table V of Ref. 24. Therefore Eqs. (15) can uniquely be transformed to the elements of $\bar{\bar{T}}$. Because of $O_1=C_1$ for the outer bands there are $\mu_T=6$ nonzero tensor elements, but only 5 nonzero IP's. Therefore we use the approximation

$$(\bar{\bar{T}})_{\tilde{x}\tilde{z}}=(\bar{\bar{T}})_{\tilde{y}\tilde{z}}$$

(16)

to reduce μ_T with the following arguments. (i) The off-diagonal tensor elements of a stretch mode generally are considerably smaller than the diagonal elements. Therefore such approximations will produce only small errors. (ii) If the axial symmetry around $\vec{p}_{OH}\|\tilde{z}$ was retained in the defect structure, the two elements of Eq. (16) would be identical and independent from $(\bar{\bar{T}})_{x,y}$ solely because of symmetry arguments.

From the intensities in Table VIII and the relations discussed here we obtain

$$\bar{\bar{T}}(v_A,II)=\pm\begin{bmatrix} \pm1.57 & -0.61 & +0.20 \\ -0.61 & +(0.27) & +0.20 \\ +0.20 & +0.20 & +1.00 \end{bmatrix} ,$$

$$\bar{\bar{T}}(v_B,III)=\pm\begin{bmatrix} +(0.38) & & -0.19 \\ & +1.06 & \\ -0.19 & & +1.00 \end{bmatrix} ,$$

(17)

$$\bar{\bar{T}}(v_C,I)=\pm\begin{bmatrix} \pm1.54 & -0.42 & +0.19 \\ -0.42 & +(0.15) & +0.19 \\ +0.19 & +0.19 & +1.00 \end{bmatrix} .$$

The tensor elements are normalized such that the $\tilde{z},\tilde{z}$ components become unity. We omit to give the error in-

tervals for the tensor elements. They follow from the experimental uncertainties of the IP's, and are approximately ±0.10 in the units used in Eq. (17).

As a surprising result and as a common feature of all three tensors we note that the polarizability changes along the axis parallel to the second octahedron edge, perpendicular to $\vec{p}_{OH}$, are particularly small. In Eqs. (17) the corresponding elements are set in parentheses ($\cdots$). Contrarily, the diagonal elements for the third molecular axis, along the cubic crystal axis, are even larger than those for the dipole axis. The directions connected to large diagonal tensor elements point towards other oxygen ions. This indicates that the electronic orbitals of the oxygen ions are strongly oriented and very easily polarizable in these directions. In this way, the OH defect observed by means of Raman scattering can be regarded as a sensitive probe for local electronic susceptibilities in the lattice.

C. Hydrogen in $K_{1-x}Li_xTaO_3$

1. Hydrogen centers in $K_{1-x}Li_xTaO_3$

In $K_{1-x}Li_xTaO_3$ (KTL) a phase transition is induced due to the off-center displacement of the Li ions.[44,45] It is obviously established that for $T < T_c$ the Li ions occupy off-center positions[44] displaced along the cubic axes. Kleemann and co-workers[45,47] interpret the transition to be of the order-disorder type into a polar ferroelectric phase; Höchli and co-workers[44,48] consider the $K_{1-x}Li_xTaO_3$ system as a model substance for a dipole glass characterized by the absence of a long range order.

A splitting of the single cubic OH band into three components has been observed for the $x = 0.023$ sample used in the present Raman experiments; see Fig. 12. In contrast to the notation for $SrTiO_3$ the subbands in KTL shall be denoted $\bar{\nu}_1 < \bar{\nu}_2 < \bar{\nu}_3$. A static external electric field $\vec{E}_{stat}\|[001](E_{stat} > 3$ kV/cm) applied upon cooling below T_c leads to a pronounced dichroism of the central line $\bar{\nu}_2$ with maximum absorption for light polarization
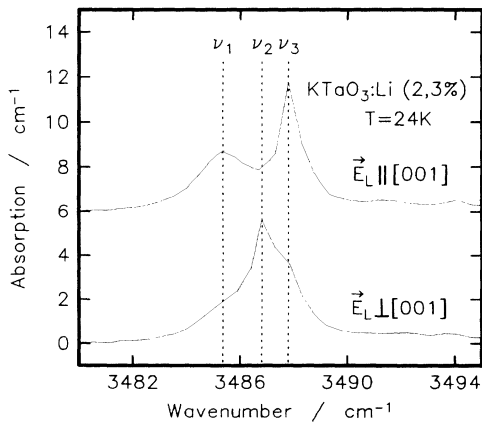

FIG. 12. Polarized ir absorption spectra of the OH stretch mode in a $K_{1-x}Li_xTaO_3$ $(x = 0.023)$ crystal, which was poled with a static external field $\vec{E}_{stat}\|[001], E_{stat} > 3$ kV/cm upon cooling below T_c.

$\vec{E}_L\perp[001]$. This points to an almost complete poling by the external electric field. The poling is retained even after switching off the field $\vec{E}_{stat}$ below T_c. The outer two lines $\bar{\nu}_1$ and $\bar{\nu}_3$ possess an isotropic absorption.

The splitting and the polarization of the three components of the OH band in KTL resemble the situation in $SrTiO_3$, although the structure of the tetragonal phase is different. The splitting in KTL is due to the interaction $\vec{p}_{OH}\cdot\vec{P}$ of the OH dipole moment $\vec{p}_{OH}$ with the macroscopic inner polarization $\vec{P}$ resulting from the off-center Li_K ions. The low and high energetic components $\bar{\nu}_1$ and $\bar{\nu}_3$ in KTL are assigned to those sites with $\vec{p}_{OH}$ components antiparallel or parallel to the polarization $\vec{P}$. For the central line we have sites with $\vec{p}_{OH}\perp\vec{P}$. A distinction similar to that for sites IIIa and IIIb in $SrTiO_3$ (see Fig. 9) is therefore not necessary.

2. Predictions of the BT method and results

The effect of Li doping or of the inner polarization on the local symmetry cannot be predicted. If the influence of Li_K can be neglected, the vertical mirror plane $\sigma(010)$ is preserved during the phase transition for sites I and II (OE) as well as for sites 3 and 4 (CF). The local symmetry of the outer bands $\bar{\nu}_1$ and $\bar{\nu}_3$ is at least $O'_1 = C_{1h}(010)$ with $s_3 = 0$. Contrarily, a strong influence of Li ions would destroy the reflection symmetry and a nonzero s_3 is expected.

If the polar character of KTL has only a minor influence on the local symmetry of hydrogen, the horizontal mirror plane $\sigma(001)$ is preserved for sites III (OE) and sites 1 and 2 (CF), inducing the IP relation $s_{12} = 0$. A strong influence of the nonpolar character would destroy the horizontal reflection symmetry and $s_{12}\neq 0$ would result.

We note that in contrast to $SrTiO_3$ the horizontal $\sigma(001)$ or $\sigma(010)$ mirror planes do not allow a decision because of equal IP's s_i $(i = 1,2,3)$. A model discrimination is only possible in the case of a negligible influence of Li_K. In this case an additional diagonal vertical mirror plane $\sigma(110)$, i.e., $O'_1(\bar{\nu}_2,CF) = C_{2v}[110](110)(001)$, occurs for sites 1 and 2 (CF) (see Fig. 9), with an additional IP relation $r_3 = q_{1,2}(BT\ 27)$. No such diagonal mirror plane is present in the OE model. Therefore r_3 and $q_{1,2}$ are independent (BT 26).

When applying an external electric field the three characteristic IP's s_i $(i = 1,2,3)$ can only be obtained in OGP set 5. In our Raman experiments we use a $K_{1-x}Li_xTaO_3$ crystal, $x = 0.023\pm0.004$, with a $T_c = 44\pm2$ K. Unfortunately the unresolvable splitting of the subbands does not allow studies of the isolated single subbands; see Fig. 12. Neither the energetic splitting increases nor the bandwidth decreases considerably when going below the measurement temperature of 24 K to suprafluid helium temperature (1.5 K).

Again we need a monodomain crystal. Because of the spectral overlap of $\bar{\nu}_1$ and $\bar{\nu}_3$, absorption contributions to $\bar{\nu}_2$ for $\vec{E}_L\|z$ cannot be excluded. Therefore the polarization behavior of $\bar{\nu}_2$ is not a sensitive criterion for a monodomain state. SHG (second harmonic generation) experi-
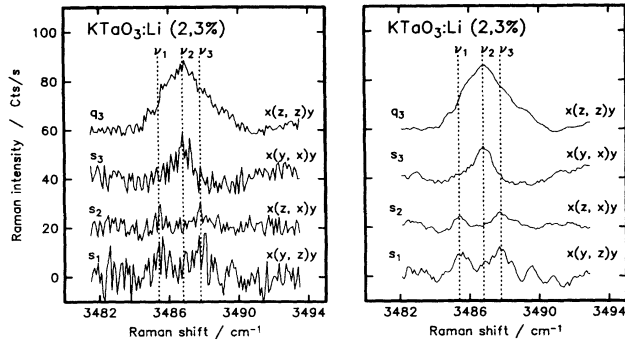
FIG. 13. Characteristic polarized Raman spectra of the OH stretch mode in the tetragonal phase of $K_{1-x}Li_xTaO_3$ ($x = 0.023$) at $T = 24$ K. Left part: unsmoothed spectra; right part: PLSC smoothed spectra.

ments similar to those described in Ref. 46 have also been performed with crystal used here and indicate an almost complete alignment of 90° domains. In Fig. 13 we present the polarized Raman spectra for the IP's $q_3 \propto I_{z,z}$, $s_3 \propto I_{x,y}$, $s_2 \propto I_{z,x}$, and $s_1 \propto I_{y,z}$. The left part shows spectra without smoothing, the right part after smoothing with the PLSC (polynomial least squares convolution) technique.[49]

Because of the strong noise and, more serious, the spectral overlap, the precise intensity ratios cannot be obtained. However, the relevant behavior of the IP's can be observed. In the spectrum $I_{z,z} \propto q_3$ all three bands overlap and yield a broad structure. This indicates that $q_3 \neq 0$ for all three lines. The IP's s_i show a complementary behavior. For the central line $\bar{v}_2$ we observe $s_1 = s_2 = 0$ and $s_3 \neq 0$; for the two outer bands $\bar{v}_1$ and $\bar{v}_3$ we find $s_1 \neq 0 \neq s_2$ and $s_3 = 0$. The IP's $q_{1,2}$ and r_3 could not be measured. According to Table IX these two IP's are nonzero for all A modes. Together with this theoretical result, we identify the tetragonal BT 24 for $\bar{v}_1$ and $\bar{v}_3$. For $\bar{v}_2$ only BT's 26 or 27 are in question. Without measuring r_3 and $q_{1,2}$ one cannot decide further between these BT's.

3. Discussion

At first we consider the BT's of the outer lines $\bar{v}_1$ and $\bar{v}_3$. From all the possible actual symmetries in Table VI of Ref. 24, to which the observed BT 24 belongs, only $O'_1 = C_{1h}(010)$ is compatible with the structure of KTL. The $\sigma(010)$ mirror plane is compatible with a collective off-center displacement of the Li_K ions along $z \| [001]$ and the influence of the external poling field. For a weak influence of the Li_K ions the $\sigma(010)$ mirror plane is expected for both the OE and CF models in KTL.

Assuming a homogeneous distribution of the Li_K, we expect that only each $N \approx 3.5$th unit cell contains one Li_K for $x = 0.023$ ($N \approx x^{-1/3}$). Thus the distance OH-Li_K is large enough to suppress the interaction of both, because the OH symmetry is dominated primarily by the Coulomb interaction with the ions in the very next environment. In contrast to $SrTiO_3$ the outer bands in KTL are of minor importance.

We turn to the behavior of $\bar{v}_2$ and use similar argu-

ments as before. The vanishing of the IP's $s_{1,2}$ indicates at least the existence of a horizontal $\sigma(001)$ mirror plane, i.e., $O'_1 = C_{1h}(001)$ or higher; compare Table IX. This appears to conflict with the polar character of the tetragonal phase of KTL, which does not possess a horizontal reflection symmetry. Even the argument that the local symmetry of hydrogen is determined only by the positions of the surrounding nearest ions, such that the influence of the off-center Li_K might be negligible, does not suffice to solve the conflict: the ferroelectric polarization induces an off-center position also of the Ta^{5+} ions. Without quantifying the Ta^{5+} displacement, Fujii and Sakudo detected a breakdown of the inversion symmetry in pure $KTaO_3$ by means of electric-field-induced SHG.[50] The size of their electric field (some kV/cm) was comparable to the polarization field in KTL.[44] The off-center displacement of Li_K; $\delta = (126 \pm 2)$ pm,[51] is about one-quarter of the lattice constant. From extended x-ray-absorption fine-structure (EXAFS) measurements the much smaller displacements of the ions in the center of the oxygen octahedron could be determined for materials closely related to $KTaO_3$:Li. For $KTaO_3$:Na Yacobi et al. found $\delta = 14$ pm along $\langle 111 \rangle$ for Ta^{5+}.[52] In $KTa_{1-x}Nb_xO_3$ with $x = 0.09$ at 70 K the value $\delta = 14.5$ pm was estimated for Nb^{5+} along $\langle 111 \rangle$.[53] Another argument in favor of the expected breakdown of the $\sigma(001)$ reflection symmetry follows from the comparison with the Raman data for $SrTiO_3$. The displacement of the O^{2-} ions due to the rotation of the oxygen octahedra ($\varphi \approx 2°$) is $\delta = 7$ pm. The related breakdown of the vertical minor plane was clearly detected in the Raman spectra in the behavior of v_A and v_C ($s_3 \neq 0$).

Now arguments shall be collected which may explain the observed Raman data for KTL. Even though $\delta_{O^{2-}}$ in $SrTiO_3$ is of the same order as the expected δ_{Ta} in KTL, the influence of these displacements on the local symmetry O'_1 of hydrogen may be much stronger in $SrTiO_3$ than in KTL. This is because in $SrTiO_3$ it is just the O^{2-} ion to which the hydrogen is bound, which changes its position. Furthermore the reconstructed Raman tensors [Eqs. (17)] in $SrTiO_3$ indicate the strong anisotropic electronic polarizability of the OH mode with a strong coupling to the oxygen sublattice. This finding and the fact that in the OE model the proton occupies a site on the O–O bond favor the assumption that O'_1 is almost completely determined by the structure of the oxygen sublattice. The oxygen sublattice preserves a horizontal reflection symmetry even in case of a tetragonal elongation along [001]. Finally the observed IP relation $s_{1,2} = 0$ for $\bar{v}_2$ in KTL may be a consequence of an accidental degeneracy of an actual BT with $s_{1,2} \neq 0$. The poor signal-to-noise (S/N) ratio of the spectra in Fig. 13 and the spectral overlap of the outer bands $\bar{v}_1$ and $\bar{v}_3$ do not allow one to prove the vanishing of $s_{1,2}$ for $\bar{v}_2$ with better accuracy.

A distinction involves a test of the equality or nonequality of r_3 and $q_{1,2}$, respectively. Such a test is hampered by the experimental constraints. However, the obviously negligible influence of the Li_K ions on the OH defect and the lattice constant in KTL, which is nearly identical to that in $SrTiO_3$, favor the application of the

OE model also for $KTaO_3$:Li. Consequently this means that the different behaviors of the tetragonal Raman IP s_3 for $SrTiO_3$ (Fig. 10) and $KTaO_3$:Li (Fig. 13) reflect the difference between the polar off-center character in the tetragonal phase of $KTaO_3$:Li and the antiferrodistortive structure of $SrTiO_3$.

D. Hydrogen in TiO_2

1. Models for the OH defect in TiO_2

Several ir absorption studies of the OH stretch mode at $\bar{v}_{OH} = 3277$ cm^{-1} in TiO_2 lead to various atomistic models proposed for the proton sites. (i) Guided by the empirically established correlation of $\bar{v}_{OH}$ with the distance R_{O-O} in an O–H $\cdots$ O configuration,[57] van Hippel et al. proposed the protons to vibrate onto those edges of the TiO_2 octahedra which do not lie in the basal (001) plane.[55] We call this the nonbasal octahedron edge (NBOE) model. The sites are illustrated in the left part of Fig. 14, which emphasizes the stacking of oxygen octahedra along the tetragonal axis of TiO_2. A dichroism perpendicular to the z axis[54,56] selects proton sites on O–O bonds within the basal plane; see the right part of Fig. 14. (ii) The site adjacent to $(\frac{1}{2},\frac{1}{2},0)$ lies on the diagonal octahedron edge, the shortest O–O bond (252 pm) oriented along [110]. We call this the basal octahedron edge (BOE) model. (iii) The site at $(\frac{1}{2},0,0)$ in the center of the open channels, which traverse the crystal parallel to the optical axis, shall be called the channel center (CC) model ($R_{O-O} = 333$ pm). Although approximate potential calculations favor the BOE model, Johnson et al. preferred the CC model.[54] Because of another empirically established correlation of the bond length $r_e = R_{O-H}$ with R_{O-O} in an O–H $\cdots$ O configuration[57] the bond lengths are expected to be $r_e = 106$ and 96 pm for the BOE and the CC models, respectively. Therefore the proton will be shifted along O–O towards either oxygen ion. (iv) The resulting proton positions a' and a'' shall be referred to as the

modified BOE (MBOE) model and (v) the sites b' and b'' as the modified CC (MCC) model. In the modified models the proton vibrates in a double well potential. For the MCC model the corresponding splitting of the OH band is expected to be smaller than 0.1 cm^{-1}, well below the room temperature linewidth (20 cm^{-1}), while for the MBOE model it would be larger than 100 cm^{-1}.

All models discussed so far have their drawbacks. The NBOE model cannot explain the strong dichroism, while the (M)BOE and the (M)CC models contradict the empirical correlation between $\bar{v}_{OH}$ and R_{O-O}. The (M)BOE and the (M)CC models can principally not be distinguished by means of polarized ir absorption, because an isotropic behavior of the dipole ensembles within the basal plane is expected and observed. From the angular dependence of the electron paramagnetic resonance (EPR) of Fe^{3+} impurities associated with protons Anderson et al. deduced the proton site to be $(0.56,0.11,0)$.[58] Elaborate potential calculations of Bates et al. yielded $(0.57,0.12,0)$.[59] Both investigations are only indirect hints in favor of the MCC model, while a conclusive spectroscopic investigation is still missing.

2. Predictions of the BT method and results

In Fig. 14 it is easy to see the different characteristic symmetry elements of the point groups O'_1 belonging to the various models. For the NBOE model there are neither mirror planes nor twofold axes; therefore $O'_1 = C_1$ with BT 21. Because rutile possesses an unpolar phase, the sites of the CC and MCC models lie within a horizontal mirror plane $\sigma(001)$, i.e., $O'_1 = C_{1h}(001)$. This induces the vanishing of the IP's $s_{1,2}$ (BT 26). The sites of the BOE and the MBOE models, which also lie in the horizontal mirror plane $\sigma(001)$ ($s_{1,2} = 0$), possess an additional vertical diagonal mirror plane $\sigma(110)$. This induces the IP relation $r_3 = q_{1,2}$. Both reflection symmetries fix the proton site on the basal octahedron edge, i.e., $O'_1 = C_{2v}[1\bar{1}0](110)(001)$. The combination of $s_{1,2} = 0$ and $r_3 = q_{1,2}$ makes up a tetragonal BT 27. In summarizing we note that all models [NBOE, (M)BOE, and (M)CC], can be discriminated by Raman experiments.

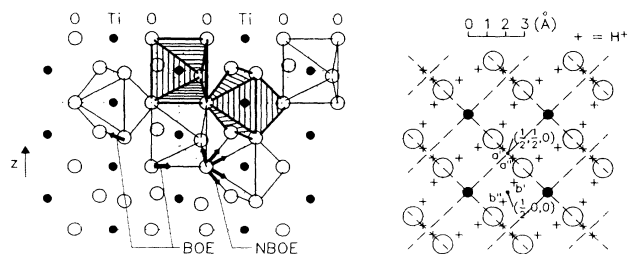Two Raman bands are clearly observable in the spectra displayed in Fig. 15. The prominent band centered at

FIG. 14. Schematic sketch of the crystal structure of TiO_2 (rutile). The left part redrawn from Ref. 55 emphasizes the octahedral arrangement of the oxygen ions. The –Ti–O–O– sequence is directed along [110] or [1$\bar{1}$0]. The right part redrawn from Ref. 58 represents a cut through the basal (001) plane. The hydrogen sites according to the NBOE and BOE models are sketched by the arrows in the left part. The sites $(\frac{1}{2},\frac{1}{2},0)$ and a',a'' of the BOE and MBOE models, respectively, as well as the sites $(\frac{1}{2},0,0)$ and b',b'' of the CC and MCC models, respectively, are indicated in the right part.
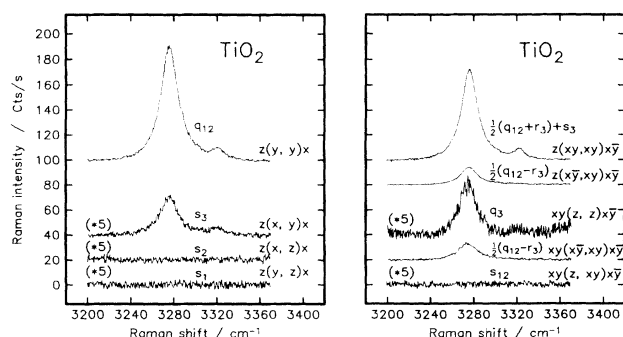

FIG. 15. Polarized Raman spectra of the OH stretch mode in TiO_2 (rutile) measured in OGP set 1 (left part) and OGP set 7 as well as OGP set 8 (right part).

TABLE X. Normalized IP's of the OH stretch mode in TiO_2 for the main band ($\bar{\nu}_0 = 3277$ cm^{-1}) and the Al^{+3}-associated satellite peak ($\bar{\nu}_{Al} = 3325$ cm^{-1}).

OH band	$\dfrac{q_{12}(\bar{\nu}_{Al})}{q_{12}(\bar{\nu}_0)}$[a]	q_{12}[b]	q_3	r_3	s_{12}	s_3	BT_{tet}
3277 cm^{-1}	100.0	100.0	8.26 ± 0.86	57.70 ± 4.4	0.0 ± 0.3	6.78 ± 0.27	26
3325 cm^{-1}	7.02 ± 1.93	100.0	8.50 ± 5.50	100.0 ± 5.0	0.0 ± 5.0	11.5 ± 6.50	27

[a]Main band $\bar{\nu}_0$ normalized to 100%.
[b]IP's $q_{1,2}$ normalized to 100%.

3277 cm^{-1} (main band) belongs to the undisturbed proton sites, while the satellite peak at 3325 cm^{-1} has been attributed to protons associated with Al^{3+} impurities.[54] From the integrated peak intensities of Fig. 15 we calculated the normalized IP's for both bands summarized in Table X.

For both bands we can directly read the characteristic IP relations $s_1 = s_2 = 0$ from the two lower spectra in the left part and the lowest spectrum in the right part of Fig. 15. For the main band the other IP's yield a BT 26. For the satellite peak we find a zero intensity for the OGP $(\vec{a},\vec{b}) = (x\bar{y},xy)$, checked in both OGP sets 7 and 8. The measurement of this intensity provides a direct and sensitive test for the characteristic behavior of the IP r_3, because one has $I_{x\bar{y},xy} = 0 \Longrightarrow r_3 = q_{1,2}$. We observe a BT 27 for the Al^{3+}-associated protons.

3. Model decision and tensor reconstruction

The existence of a horizontal mirror plane $\sigma(001)$ for the main OH band clearly excludes the old NBOE model.[55] From the result $I_{x\bar{y},xy} \neq 0$ it follows that $r_3 \neq q_1$. According to Table IX this excludes the existence of a vertical diagonal $\sigma(110)$ reflection plane and therefore the validity of the (M)BOE models. For $O_1 = C_{1h}(001)$ all dipole directions apart from the [110] or [1$\bar{1}$0] octahedron edges are compatible. Therefore the incorporation precisely along the 333 pm O–O bond across the open channels cannot be proved from our data alone. This follows from the general tendency of interstitial hydrogen to form O–H $\cdots$ O configurations, as was confirmed in other oxides, e.g., for $SrTiO_3$ (see Sec. IV B) and is strongly assumed for $LiNbO_3/LiTaO_3$.[60]

The vanishing of $I_{x\bar{y},xy}$ for the satellite peak indicates $r_3 = q_1$ and is related to an additional $\sigma(110)$ reflection plane. Accidental degeneracy of behavior types is excluded for the Al^{3+} satellite peak: a precise evaluation of the intensities in Table X for both peaks in the spectra reveals an almost constant intensity ratio independent of the scattering geometry. If this held also for $I_{x\bar{y},xy}$, then by comparison with $I_{z,z}$ the detection efficiency of the experiment would have been sufficient to detect a nonzero $I_{x\bar{y},xy}$ also for the satellite peak. Therefore we are sure that the relation $r_3 = q_{1,2}$ deduced from $I_{x\bar{y},xy} = 0$ actually reflects the $\sigma(110)$ mirror plane. Consequently we assume the Al^{3+}-associated protons to be incorporated along the basal octahedron edges according to the BOE

or MBOE model. In order to preserve the local symmetry $O_1 = C_{2v}[110](110)(001)$, the associated Al^{3+} ion must also be located on the $C_2[110]$ axis. Because of the deviating charge state of the Al^{3+} impurity on the Ti^{4+} site and the Coulomb interaction with the proton, an off-center displacement is expected. From the symmetry and the orientation of the Fe^{3+}-OH complex the displacement is likely to occur along [110]. Any displacement along this direction is compatible with the detected $C_{2v}[110]$ symmetry of the Al^{3+}-OH center. In TiO_2 we are therefore confronted with the result that Al^{3+}-associated protons possess a higher symmetry and occupy different sites than the protons on the undisturbed sites.[25]

Because of $O_1 = C_{1h}(001)$ the Raman tensor $\bar{T}$ for the main band contains only four independent elements.[24] This allows one to reconstruct $\bar{T}$ by solving Eqs. (9) without further assumptions. We transform $\bar{T}$ from the crystal frame to the defect frame $(\bar{x},\bar{y},\bar{z})$ assuming the MCC model. The proton at $b' = (0.57,0.12,0)$ is bound to the O^{2-} ion at $(0.805,0.305,0)$;[59] see Fig. 14. We select $\bar{z}\|\vec{p}_{OH}$ (the OH dipole moment), $\bar{y}\|[001]$, and $\bar{x}$ perpendicular to both. We obtain two different solutions for $\bar{T}$ from the IP's of Table X, namely,

$$\bar{\bar{T}}_I = \pm \begin{bmatrix} -2.06 & \pm0.22 & \\ \pm0.22 & \pm0.28 & \\ & & 1.00 \end{bmatrix}$$

and   (18)

$$\bar{\bar{T}}_{II} = \pm \begin{bmatrix} 1.34 & \pm0.11 & \\ \pm0.11 & \pm0.14 & \\ & & 1.00 \end{bmatrix}.$$

Both solutions show similar characteristics: (i) The polarizability changes $T_{\bar{y},\bar{y}}$ perpendicular to the basal plane and the off-diagonal tensor element $T_{\bar{x},\bar{y}}$ are comparably small. (ii) Within the basal plane, the derived polarizability $T_{\bar{x},\bar{x}}$ perpendicular to the dipole axis is even larger than the value $T_{\bar{z},\bar{z}}$ along $\vec{p}_{OH}$. This indicates a strong deviation from the case of a free OH$^-$ molecule with $C_{\infty v}$ symmetry, for which one would expect zero off-diagonal elements and $T_{\bar{x},\bar{x}} = T_{\bar{y},\bar{y}} \neq T_{\bar{z},\bar{z}}$. These findings reflect the results from the potential calculation of Bates et al.:[59] The defect structure and the significant deviations from the free molecule properties are determined by the electrostatic interaction of the proton with the surrounding lattice ions in TiO_2 rather than the O–H $\cdots$ O configuration.

E. Hydrogen in LiTaO₃/LiNbO₃

The optical, electrical, and acoustical properties are influenced by a variety of intrinsic and extrinsic defects.[61,62] The results of numerous ir spectroscopic investigations of the OH stretch mode in $LiNbO_3$ were summarized by Kovács et al.[60] Comparably few work has been published for $LiTaO_3$, e.g., Ref. 12. Earlier Raman investigations of the OH stretch mode were performed for $LiNbO_3$ (Ref. 63) and $LiTaO_3$,[64] but without the BT method extended to trigonal crystals yet available.

1. Crystal structure and proton doping

$LiNbO_3$ and $LiTaO_3$ possess the same trigonal crystal structure. Above the Curie temperature of $T_C = 1210°$ (620°) they form an unpolar phase with point group $G' = D_{3d}(\bar{3}m)$. In the polar ferroelectric phase this reduces to $G' = C_{3v}(3m)$. Between oxygen planes a stacking sequence, Nb(Ta)-vacancy-Li-Nb(Ta)-vacancy-Li of the cations, exists. One finds O–O bonds with three different O–O bond lengths in the oxygen triangles of each oxygen plane. A part of an oxygen plane is sketched in Fig. 16, where the O–O bond lengths occurring in $LiNbO_3$ and $LiTaO_3$ are indicated.

At room temperature the OH absorption band exhibits an obvious structure of subbands and it is perfectly dichroic perpendicular to the z axis. Herrington et al.[65] decomposed the spectrum into two bands, which were attributed to the shortest O–O bonds in two nonequivalent local environments, in particular the sites labeled 1 and 2 in Fig. 16. Kovács et al.[66] proposed a three-band decomposition, where the three subbands are attributed to proton sites on the three O–O bonds with three different bond lengths. Because these bonds are embedded in different cation environments, they assumed the sites (1, 2), (3, 4), (5, 6) from Fig. 16 to be energetically degenerate. A description of the band using four transitions leads to a considerable improvement of the fit of the band shape compared to that using only three transitions.[60]

The intrinsic defects are explicitly taken into account in the model of Birnie.[67] When Nb(Ta) ions occupy vacant Li sites between adjacent vacant Nb sites, then a
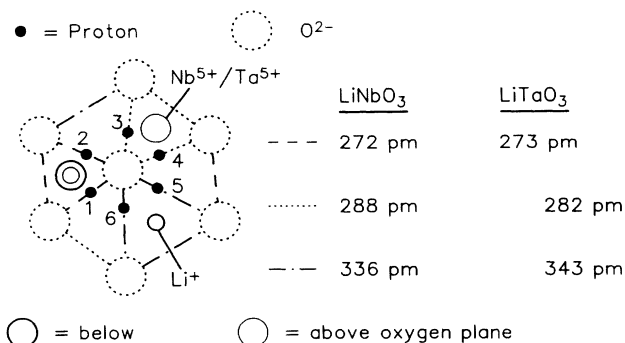
stacking sequence results, in which two sequentially neighboring centers of oxygen octahedra are not occupied by cations. The preferred site of the proton would be in the intermediate oxygen plane for simple electrostatic reasons.[67]

Because of the isotropy of the absorption in the horizontal (001) plane, the direction of the potential minimum for the incorporation of the proton cannot be concluded from ir spectroscopy for all models discussed.

2. Symmetry aspects and results

Because of the different cation environment and the absence of a horizontal mirror plane $\sigma(001)$ in the ferroelectric room temperature phase, all models result in the same local symmetry of the defect, $O_1 = C_1$. In all cases the minimum trigonal BT 12 of Table IV is expected; therefore a distinction between the models based on polarized Raman measurements is not possible.

But the local environment in the model of Birnie[67] might simulate a local $\sigma(001)$ reflection symmetry. A horizontal mirror plane $\sigma(001)$ would effect the form of the Raman tensor, such that $T_{12} = T_{22} = 0$ (see Table V of Ref. 24). According to Eq. (11) this would induce the IP relation $s_1 = s_2 \equiv s_{1,2} = 0$.

Our investigation includes a reexamination of the Raman data of Refs. 63 for $LiNbO_3$ and Ref. 64 for $LiTaO_3$. To avoid difficulties with intensity ratio changes due to proton doping we measured undoped $LiTaO_3$ samples. The resultant spectra are displayed in Fig. 17. Redundant checks were performed in the OGP sets 1, 2, and 5 in order to compensate for different detection efficiencies arising from the pronounced fanning of the laser beam due to the photorefractive effect ("optical damage") in OGP's with $\vec{a}\|z$. The measured values of the IP's q_i and s_i ($i = 1,2,3$) are summarized in Table XI and compared with the data of Ref. 64 for undoped and proton- and deuteron-doped $LiTaO_3$.

3. Discussion

From Fig. 17 we read $s_{1,2} \neq 0$, ruling out the model of Birnie[67] expecting $s_{1,2} = 0$. This holds also for proton-

FIG. 16. Schematic representation of an oxygen (001) plane in $LiNbO_3$/$LiTaO_3$ with the three O–O bond lengths given for both materials. The original figure from Ref. 60 was slightly modified.
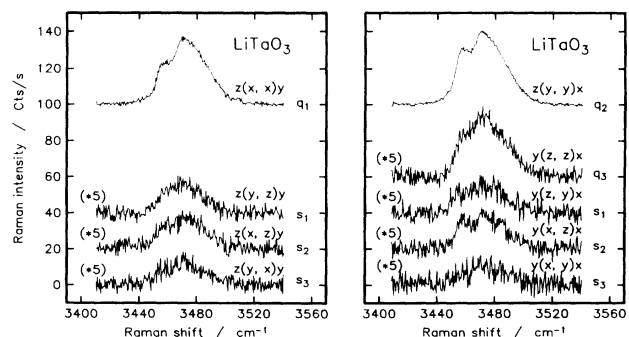

FIG. 17. Polarized Raman spectra of the OH stretch mode in undoped $LiTaO_3$ crystals measured at room temperature.

TABLE XI. Summary of IP's for the OH stretch mode in $LiTaO_3$ and comparison with the results from Ref. 64.

Experiment	$q_{1,2}$	q_3	$s_{1,2}$	s_3
$LiTaO_3$, as grown[a]	100 ± 3	18 ± 3	8.1 ± 1.0	5.3 ± 0.6
$LiTaO_3$, as grown[b]	100 ± 40	50 ± 25	<10	<10
$LiTaO_3$, H doped[b]	100 ± 9	8 ± 2	5 ± 3	5 ± 3
$LiTaO_3$, D doped[b]	100 ± 5	9 ± 2	10 ± 3	4 ± 3

[a]This work.
[b]Reference 64.

and deuteron-doped $LiTaO_3$ (Ref. 64) and $LiNbO_3$ samples with various Li/Nb composition ratios[63] and excludes a horizontal mirror plane $\sigma(001)$ even in local approximation. Therefore the symmetry of the OH stretch mode reflects the different cation environment above and below the oxygen plane.

The results $s_{1,2}\neq0$ and $s_3\neq0$ also exclude the trigonal BT 25 related to $O_1=C_3[001]$ or $D_3[001]$, i.e., an orientation of the OH dipole along the trigonal axis. As a result we conclude that the *symmetry* of the OH stretch mode in $LiNbO_3$ and $LiTaO_3$ is as low as $O_1=C_1$, preventing any stringent model discrimination in the $LiNbO_3$ family. This finding can be generalized: Because of the comparable low symmetry G' of trigonal crystals, there are only few possible different symmetries $O'_1\subset G'$ for a local mode to be distinguished. Therefore an extension and application of the BT theory to still lower symmetric crystals, such as the orthorhombic crystal system, does not appear very promising.

V. SUMMARY AND PERSPECTIVES

The scope of the present report is the investigation of hydrogen defects in a variety of prototype oxidic crystals by means of polarized Raman scattering from the OH stretch mode. The Raman intensities reflect the symmetry of the dynamical mode. The theoretical basis necessary for the interpretation of the spectra and the basic experimental requirements for the performance of conclusive polarized Raman measurements are described generally and independent of any specific defect system. Then the focus is turned to hydrogen defects in the perovskite systems ($SrTiO_3, KTaO_3, K_{1-x}Li_xTaO_3$), the rutile system ($TiO_2$), and the $LiNbO_3/LiTaO_3$ family. We discuss the specific experimental constraints related with these systems. Then we put the emphasis on the interpretation of the Raman spectra in the framework of the developed theoretical method.

The underlying theory is the Raman behavior-type (BT) method introduced recently for cubic crystals.[22] We have extended the method to tetragonal[24] and trigonal[26] systems. A set of suitable quantities, the so-called intensity parameters (IP's), is introduced. The IP's are related in to the polarized intensities $I_{\vec{a},\vec{b}}$, which depend on the polarization vector of the incident ($\vec{a}$) and scattered ($\vec{b}$) light. The symmetry-induced form of the Raman tensor leads to simple algebraic relations between the IP's. The set of these relations is called the actual BT of a mode.

The IP relations can be checked in an experiment. From these data all those possible actual symmetries of a mode can be excluded for which the actual BT is not compatible with the observed BT. The method consists of an application of a set of extensive tables, which contain the results of *a priori* calculations of the actual BT, for all possible modes with all irreducible representations compatible with the crystal symmetry. The calculations include symmetry considerations only.

Lowering of the cubic crystal symmetry leads to a decrease of orientational averaging. The discriminative power of the method is considerably increased. On the other hand the optical anisotropy and birefringence in the uniaxial (tetragonal and trigonal) systems necessitate additional scattering geometries to exploit the complete symmetry information. In particular, all A-type modes, to which the OH stretch mode belongs, possess a different BT for each representative symmetry.

Raman measurements of the OH stretch mode band in differently prepared $SrTiO_3$ crystals and $K_{1-x}Li_xTaO_3$ in different compositions ($x=0,0.018,0.023$) aimed at a decision between three models discussed in the literature for the hydrogen incorporation in perovskite crystals.

The cubic-to-tetragonal phase transition in $SrTiO_3$ induces a splitting of the single cubic OH band into three components $v_A<v_B<v_C$. Application of the BT method to this component favors the octahedron edge model with the proton vibrating along the O–O bonds of the oxygen octahedron.

The measurement of all independent tetragonal IP's for all three subbands in $SrTiO_3$ allowed us to reconstruct the molecular Raman tensors in the defect frames of reference related to the different sites. The OH defect becomes a probe of local dielectric susceptibilities. The polarizability changes are extraordinarily strong on the octahedron edge parallel to the dipole moment $\vec{p}_{OH}$ and the (former cubic) axis perpendicular to $\vec{p}_{OH}$. They are surprisingly weak on the octahedron edge perpendicular to $\vec{p}_{OH}$.

The OH defect has also been investigated in mono-domain tetragonal $K_{1-x}Li_xTaO_3$ ($x=0.023$). For $x>x_c=0.022$ the Li_K ions freeze in an off-center position along the [001] axis. As in $SrTiO_3$, the OH mode splits into three components. The analysis of the polarized Raman data shows characteristic IP relations resulting in a vertical mirror plane $\sigma(010)$ for the sites of the outer bands and a horizontal mirror plane $\sigma(001)$ for the central band. This result could not *a priori* predicated,

because the effect of the Li_K impurities on the local symmetry of the protons could not be estimated. A statistical distribution of the Li_K ions might destroy the vertical mirror plane $\sigma(010)$ and the polar off-center displacement contradicts the horizontal reflection symmetry $\sigma(001)$. The present Raman results seem to indicate that the *local* symmetry experienced by the OH defect is only determined by the configuration of the nearest neighbors or the oxygen sublattice and not by the *global* symmetry of the lattice. Assuming the OE model to hold also for $K_{1-x}Li_xTaO_3$, then the different behavior of the IP's for the outer two bands v_1, v_3 with respect to that of v_A, v_C in $SrTiO_3$ is able to reflect the difference between the polar off-center character in $K_{1-x}Li_xTaO_3$ [$\sigma(010) \rightarrow s_3 = 0$] and the antiferrodistortive structure of $SrTiO_3$ [breakdown of $\sigma(010) \rightarrow s_3 = 0$] in the Raman spectra of OH.[21]

For the specific tetragonal structure of rutile (TiO_2) the application of the BT method appears to be especially efficient and successful. For each of the models for the incorporation of hydrogen proposed in the literature another O–O bond with characteristic local symmetry is related to, see Ref. 25. For the main band and the Al^{3+}-associated satellite peak we found IP relations exclude the so-labeled nonbasal octahedron edge (NBOE) model. The absence of further IP relations also excludes the basal octahedron edge (BOE) and the modified (MBOE) models, $O_1'(BOE) = C_{2v}[110]$. The observed $C_{1h}(001)$ symmetry is in accordance with the channel center (CC) model or the modified (MCC) version, supported by EPR investigations and theoretical potential calculations. In contrast to this we found for the Al^{3+}-associated band an additional diagonal mirror plane $\sigma(110)$. This points to a $C_{2v}[110](1\bar{1}0)(001)$ symmetry, which is characteristic for the BOE or MBOE model.

Furthermore, Raman measurements were performed with $LiTaO_3$ crystals representative of the $LiNbO_3$ family. Theoretical analysis based on the extension of the BT method to trigonal systems shows that some of the characteristic trigonal IP relations become more complicated than those in cubic and tetragonal crystals. Because of this, the IP relation belonging to a vertical $\sigma(100)$ mirror plane could not be tested with sufficient experimental precision. According to the low symmetry of the $LiTaO_3$ lattice the Raman data indicate a $O_1' = C_1$

site symmetry. This does not allow any conclusion concerning a specific dipole site or dipole direction. According to the model of Birnie, which explicitly includes the intrinsic Li-deficient structure, a horizontal $\sigma(001)$ reflection symmetry might be expected in local approximation. This notion can be excluded from the Raman data.

Some interesting theoretical and experimental problems arise from the results of the present investigations. On the theoretical side the strong increase of the discriminative power of the BT method upon lowering the cubic crystal symmetry renders an extension to hexagonal crystals, $G' = D_{6h}(6/mmm)$, $h' = 24$, highly appreciable. Because of $D_{6h} = D_6 \times i$, the treatment can be reduced to $G = D_6(622)$, $h = 12$. This point group contains a variety of subgroups, i.e., possible representative symmetries of local modes, which may be distinguished with Raman experiments. In trigonal crystals the low symmetry and the resulting small number of distinguishable representative modes indicate that further extension to still lower symmetric systems, such as orthorhombic crystals, does not appear to be fruitful.

From the experimental point of view BT investigations of the OH stretch mode in $BaTiO_3$ would be interesting. The material is tetragonal at room temperature. A speculation arose from ir absorption data that diverging from the OE model the protons might occupy sites according to the CA model.[68,69] An interesting question arises also in $SrTiO_3$ concerning the problem of the strength of the influence of the global symmetry of the crystal on the local symmetry relevant for the hydrogen defect. In this incipient ferroelectric material ferroelectric phase transitions are induced upon the application of uniaxial stress, e.g., along [100] or [010].[42] Similar to $K_{1-x}Li_xTaO_3$ the question arises whether the polar character is able to break the horizontal mirror planes of the OH defect. Possible comparisons with the $LiNbO_3/LiTaO_3$ systems may arise in the trigonal phase induced upon pressure on the (111) planes.[70]

ACKNOWLEDGMENT

[1] O. W. Johnson, J. DeFord, and J. W. Shaner, J. Appl. Phys. **44**, 3008 (1973).

[2] J. B. Bates and R. A. Perkins, Phys. Rev. B **16**, 3713 (1977).

[3] H. Engstrom, J. B. Bates, J. C. Wang, and M. M. Abraham, Phys. Rev. B **21**, 1520 (1980).

[4] H. Engstrom, J. B. Bates, and L. A. Boatner, J. Chem. Phys. **73**, 1073 (1980).

[5] R. Gonzalez, M. M. Abraham, L. A. Boatner, and Y. Chen, J. Chem. Phys. **78**, 660 (1983).

[6] R. Gonzalez, Y. Chen, K. L. Tsang, and G. P. Summers, Appl. Phys. Lett. **41**, 739 (1982).

[7] Y. Chen, R. Gonzalez, and K. L. Tsang, Phys. Rev. Lett. **53**,

1077 (1984).

[8] S. Klauer, M. Wöhlecke, and S. Kapphan, Phys. Rev. B **45**, 2786 (1992).

[9] J. Jackel, A. M. Glass, G. E. Peterson, C. E. Rice, D. H. Olson, and J. J. Veselka, J. Appl. Phys. **55**, 269 (1984).

[10] M. DeMicheli, J. Botineau, P. Sibillot, D. B. Ostrowsky, and M. Papuchon, Opt. Commun. **42**, 101 (1983).

[11] H. Vormann, G. Weber, S. Kapphan, and E. Krätzig, Solid State Commun. **40**, 453 (1981).

[12] R. G. Smith, D. B. Fraser, R. T. Denton, and T. C. Rich, J. Appl. Phys. **39**, 4600 (1968).

[13] R. Waser, Z. Naturforsch. **42a**, 1357 (1987).

[14]A. S. Barker and A. J. Sievers, Rev. Mod. Phys. **47**, 1 (1975).

[15]A. F. W. Klukhuhn, J. Bruining, B. Klootwijk, and J. v. d. Elsken, Phys. Rev. Lett. **25**, 380 (1970).

[16]S. Kapphan, J. Koppitz, and G. Weber, Ferroelectrics **25**, 585 (1980).

[17]S. Jandl, D. Houde, Y. Lépine, and J. L. Brebner, Ferroelectrics **38**, 805 (1981).

[18]J. L. Brebner, S. Jandl, and Y. Lépine, Phys. Rev. B **23**, 3816 (1981).

[19]G. Weber, S. Kapphan, and M. Wöhlecke, Phys. Rev. B **34**, 8406 (1986).

[20]D. Houde, Y. Lépine, C. Pépin, S. Jandl, and J. L. Brebner, Phys. Rev. B **35**, 4948 (1987).

[21]S. Klauer, and M. Wöhlecke, Phys. Rev. Lett. **68**, 3212 (1992).

[22]J. F. Zhou, E. Goovaerts, and D. Schoemaker, Phys. Rev. B **29**, 5509 (1984).

[23]W. Joosen and D. Schoemaker, J. Phys. Chem. Solids **51**, 821 (1990).

[24]S. Klauer and M. Wöhlecke, Phys. Rev. B **46**, 740 (1992).

[25]S. Klauer and M. Wöhlecke, Europhys. Lett. **20**, 439 (1992).

[26]S. Klauer, Ph.D. thesis, Universität Osnabrück, Germany, 1992.

[27]The complete set of tables compiled for trigonal systems equivalent to those for cubic (Ref. 22) and tetragonal (Ref. 24) crystals can be obtained from the authors upon request.

[28]W. Hayes and R. Loudon, *Scattering of Light by Crystals* (Wiley-Interscience, New York, 1978).

[29]D. A. Long, *Raman Spectroscopy* (McGraw-Hill, New York, 1977).

[30]J. G. Pescoe, W. R. Fenner, and M. V. Klein, J. Chem. Phys. **60**, 4208 (1974).

[31]H. Fleurent, W. Joosen, and D. Schoemaker, Phys. Rev. B **38**, 6257 (1988).

[32]M. Born and E. Wolf, *Principles of Optics,* 5th ed. (Pergamon Press, Oxford, 1975).

[33]S. Klauer and M. Wöhlecke, Meas. Sci. Technol. **3**, 647 (1992).

[34]N. Schmidt, K. Betzler, M. Grabs, S. Kapphan, and F. Klose, J. Appl. Phys. **65**, 1253 (1989).

[35]H. Hesse and S. Kapphan, Phys. Status Solidi A **50**, K243 (1978).

[36]H. Fleurent, Ph.D. thesis, University of Antwerp, Belgium, 1990.

[37]A. Jovanović, M. Wöhlecke, and S. Kapphan, Radiat. Eff. Defects Solids **119-121**, 785 (1991).

[38]A. Jovanović, Ph.D. thesis, Universität Osnabrück, 1990.

[39]A. Gröne, M. Wöhlecke, S. Kapphan, and R. Waser, Ferroelectrics **107**, 97 (1990); **107**, 1343 (1990).

[40]G. Shirane and Y. Yamada, Phys. Rev. **177**, 858 (1969).

[41]M. E. Lines and A. M. Glass, *Principles and Applications of Ferroelectrics and Related Materials* (Clarendon, Oxford, 1977).

[42]H. Uwe and T. Sakudo, Phys. Rev. B **13**, 271 (1976).

[43]S. Klauer and M. Wöhlecke, Ferroelectrics **125**, 385 (1992).

[44]J. J. v. d. Klink, D. Rytz, F. Borsa, and U. T. Höchli, Phys. Rev. B **27**, 89 (1983).

[45]H. Schremmer, W. Kleemann, and D. Rytz, Phys. Rev. Lett. **62**, 1896 (1989).

[46]P. Voigt, H. Hesse, and S. Kapphan, in *Proceedings of the 20th Spring Conference on Ferroelectricity,* Güntersberge, edited by G. Schmidt and G. Sorge (Martin-Luther-Universität, Helle, 1992).

[47]W. Kleemann, S. Kütz, and D. Rytz, Europhys. Lett. **4**, 239 (1987).

[48]U. T. Höchli, K. Knorr, and A. Loidl, Adv. Phys. **39**, 404 (1990).

[49]K. L. Ratzlaff, *Introduction to Computer-Assisted Experimentation* (Wiley, New York, 1987).

[50]Y. Fujii and T. Sakudo, Phys. Rev. B **13**, 1161 (1976).

[51]J. J. v. d. Klink and S. N. Khanna, Phys. Rev. B **29**, 2415 (1984).

[52]Y. Yacobi, J. Mustre DeLeon, E. A. Stern, J. J. Rehr, and B. Rechav (unpublished).

[53]O. Hanske-Petitpierre, Y. Yacobi, J. Mustre DeLeon, E. A. Stern, and J. J. Rehr, Phys. Rev. B **44**, 6700 (1991).

[54]O. W. Johnson, W. D. Ohlsen, and P. I. Kingsbury, Phys. Rev. **175**, 1102 (1968).

[55]A. von Hippel, J. Kalnajs, and W. B. Westphal, J. Phys. Chem. Solids **23**, 779 (1962).

[56]G. J. Hill, Br. J. Appl. Phys. **1**, 1151 (1968).

[57]G. C. Pimentel and A. L. McClellan, *The Hydrogen Bond* (Freeman, San Francisco, 1960), Chap. 3.

[58]P. O. Andersson, E. L. Kollberg, and A. Jelenski, Phys. Rev. B **8**, 4956 (1973).

[59]J. B. Bates, J. C. Wang, and R. A. Perkins, Phys. Rev. B **19**, 4130 (1979).

[60]L. Kovács, M. Wöhlecke, A. Jovanović, K. Polgár, and S. Kapphan, J. Phys. Chem. Solids **52**, 797 (1991).

[61]A. Räuber, in *Current Topics in Materials Science,* edited by E. Kaldis (North-Holland, Amsterdam, 1978), Vol. 1.

[62]O. F. Schirmer, O. Thiemann, and M. Wöhlecke, J. Phys. Chem. Solids **52**, 185 (1991).

[63]A. Jovanović, S. Kapphan, and M. Wöhlecke, Cryst. Lattice Defects Amorph. Mater. **15**, 137 (1987).

[64]H. P. Winkler, diploma thesis, Universität Osnabrück, 1988.

[65]J. R. Herrington, B. Dischler, A. Räuber, and J. Schneider, Solid State Commun. **12**, 351 (1973).

[66]L. Kovács, V. Szalay, and R. Capelletti, Solid State Commun. **52**, 1029 (1984).

[67]D. P. Birnie, SPIE **968**, 81 (1988).

[68]S. Kapphan and G. Weber, Ferroelectrics **37**, 673 (1981).

[69]A. Jovanović, M. Wöhlecke, S. Kapphan, A. Maillard, and G. Godefroy, J. Phys. Chem. Solids **50**, 623 (1989).

[70]W. J. Burke, R. J. Pressley, and J. C. Slonczewski, Solid State Commun. **9**, 121 (1971).